

The Astrophysical Journal, **554**, 778-802
with minor errors corrected in Table 6 and Fig. 16

Infrared Emission from Interstellar Dust II. The Diffuse Interstellar Medium

Aigen Li and B.T. Draine

Princeton University Observatory, Peyton Hall, Princeton, NJ 08544, USA;
agli@astro.princeton.edu, draine@astro.princeton.edu

ABSTRACT

We present a quantitative model for the infrared emission from dust in the diffuse interstellar medium. The model consists of a mixture of amorphous silicate grains and carbonaceous grains, each with a wide size distribution ranging from molecules containing tens of atoms to large grains $\gtrsim 1$ micron in diameter. We assume that the carbonaceous grains have polycyclic aromatic hydrocarbon (PAH)-like properties at very small sizes, and graphitic properties for radii $a \gtrsim 50\text{\AA}$. On the basis of recent laboratory studies and guided by astronomical observations, we propose “astronomical” absorption cross sections for use in modeling neutral and ionized PAHs from the far ultraviolet to the far infrared. We also propose modifications to the far-infrared emissivity of “astronomical silicate”.

We calculate energy distribution functions for small grains undergoing “temperature spikes” caused by stochastic absorption of starlight photons, using realistic heat capacities and optical properties. Using a grain size distribution consistent with the observed interstellar extinction, we are able to reproduce the near-IR to submillimeter emission spectrum of the diffuse interstellar medium, including the PAH emission features at 3.3, 6.2, 7.7, 8.6, and $11.3\mu\text{m}$. The model is compared with the observed emission at high Galactic latitudes as well as in the Galactic plane, as measured by the COBE/DIRBE, COBE/FIRAS, IRTS/MIRS, and IRTS/NIRS instruments. The model has 60×10^{-6} of C (relative to H) locked up in PAHs, with 45×10^{-6} of C in a component peaking at $\sim 6\text{\AA}$ ($N_C \approx 100$ carbon atoms) to account for the PAH emission features, and with 15×10^{-6} of C in a component peaking at $\sim 50\text{\AA}$ to account for the $60\mu\text{m}$ flux. The total infrared emission is in excellent agreement with COBE/DIRBE observations at high galactic latitudes, just as the albedo for our grain model is in accord with observations of the diffuse galactic light. The aromatic absorption features at $3.3\mu\text{m}$ and $6.2\mu\text{m}$ predicted by our dust model are consistent with observations.

We calculate infrared emission spectra for our dust model heated by a range of starlight intensities, from 0.3 to 10^4 times the local interstellar radiation field, and we tabulate the intensities integrated over the SIRTf/IRAC and MIPS bands. We also provide dust opacities tabulated from the extreme ultraviolet to submillimeter wavelengths.

Subject headings: dust, extinction — infrared: ISM: continuum — infrared: ISM: lines and bands — ISM: abundances — radiation mechanisms: thermal — ultraviolet: ISM

1. Introduction

It has been 70 years since Trumpler’s discovery of color excesses provided the first definitive proof of the existence of interstellar dust (Trumpler 1930); however, many aspects of the nature of interstellar

dust still remain unclear. Our knowledge of the composition of interstellar grains is based mainly on their spectroscopic absorption/emission features and observed elemental depletions. The most generally accepted view is that interstellar grains consist of amorphous silicates and some form of carbonaceous materials; the former inferred from the $9.7\mu\text{m}$ Si-O stretching mode and $18\mu\text{m}$ O-Si-O bending mode absorption features in interstellar regions as well as the fact that the cosmically abundant heavy elements such as Si, Fe, Mg are highly depleted; the latter mainly inferred from the strongest interstellar absorption feature – the 2200\AA hump – and the fact that silicates alone are not able to provide enough extinction.

The dust sizes, inferred from the wavelength-dependent interstellar extinction and polarization curves, may be separated into two domains – 1) radii $a > 0.02\mu\text{m}$, which includes the “classical” grains (with $a \gtrsim 0.1\mu\text{m}$), which are primarily responsible for the extinction, polarization and scattering at visible wavelengths; and 2) the “very small grain” component (with $a < 0.02\mu\text{m}$) which contribute importantly to the extinction in the vacuum-ultraviolet. While the size distribution for the “classical grain” component is relatively well constrained by fitting the observed interstellar extinction curve for an assumed dust composition, our knowledge of the size distribution for the “very small grain” component is much poorer, due to the fact that, for $\lambda \gtrsim 0.1\mu\text{m}$, these very small grains are in the Rayleigh limit and their extinction cross sections per unit volume are independent of size, so that the observed UV/far-UV extinction curve only constrains the total volume (mass) of this grain component.

Forty-five years ago, Platt (1956) proposed that very small grains or large molecules with radii $\lesssim 10\text{\AA}$ may be present in interstellar space. Donn (1968) further proposed that polycyclic aromatic hydrocarbon-like “Platt particles”, may be responsible for the UV interstellar extinction. However, the inability to determine the detailed optical properties of “Platt particles” and the limited observational information on the UV/far-UV interstellar extinction forestalled further development of these ideas (Greenberg 1960).

Since the 1980s, an important new window on the “very small grain component” has been opened by infrared (IR) observations. The near-IR continuum emission of reflection nebulae (Sellgren, Werner, & Dinerstein 1983) and the 12 and $25\mu\text{m}$ “cirrus” emission detected by the *Infrared Astronomical Satellite* (IRAS) (Boulanger & Péroult 1988) explicitly indicated the presence of a very small interstellar dust component since large grains (with radii $\sim 0.1\mu\text{m}$) heated by diffuse starlight emit negligibly at such short wavelengths, whereas very small grains (with radii $\lesssim 0.01\mu\text{m}$) can be transiently heated to very high temperatures ($\gtrsim 1000$ K depending on grain size, composition, and photon energy) as first pointed out by Greenberg (1968). Subsequent measurements by the *Diffuse Infrared Background Experiment* (DIRBE) instrument on the *Cosmic Background Explorer* (COBE) satellite confirmed this and detected additional broadband emission at 3.5 and $4.9\mu\text{m}$ (Arendt et al. 1998).

More recently, spectrometers aboard the *Infrared Telescope in Space* (IRTS) (Onaka et al. 1996; Tanaka et al. 1996) and the *Infrared Space Observatory* (ISO) (Mattila et al. 1996) have shown that the diffuse interstellar medium radiates strongly in emission features at 3.3 , 6.2 , 7.7 , 8.6 , and $11.3\mu\text{m}$. These emission features, first seen in the spectrum of the planetary nebulae NGC 7027 and BD+30°3639 (Gillett, Forrest, & Merrill 1973), have been observed in a wide range of astronomical environments including planetary nebulae, protoplanetary nebulae, reflection nebulae, HII regions, circumstellar envelopes, and external galaxies (see Tielens et al. 1999 for a review). Often referred to as “unidentified infrared” (UIR) bands, these emission features are now usually attributed to polycyclic aromatic hydrocarbons (PAHs) which are vibrationally excited upon absorption of a single UV/visible photon (Léger & Puget 1984; Allamandola, Tielens, & Barker 1985) although other carriers have also been proposed such as hydrogenated amorphous carbon (Duley & Williams 1981; Borghesi, Bussolletti, & Colangeli 1987; Jones, Duley, & Williams 1990), quenched carbonaceous composite (Sakata et al. 1990), coal (Papoular et al. 1993), fullerenes (Webster 1993), and

interstellar nanodiamonds with sp^3 surface atoms reconstructed to sp^2 hybridization (Jones & d’Hendecourt 2000). The emission mechanism proposed for the UIR bands – UV excitation of gas-phase PAHs followed by internal conversion and IR fluorescence – is supported by laboratory measurements of the IR *emission* spectra of gas-phase PAH molecules (Cherchneff & Barker 1989; Brenner & Barker 1989; Kurtz 1992; Cook et al. 1998) and by theoretical investigations of the heating and cooling processes of PAHs in interstellar space (Allamandola, Tielens, & Barker 1989; Barker & Cherchneff 1989; d’Hendecourt et al. 1989; Draine & Li 2001).

By far the most extensively modelled dust property is the interstellar extinction curve. Existing grain models for the diffuse interstellar medium (see Witt 2000 for a recent review) are mainly based on an analysis of extinction (Mathis, Rumpl, & Nordsieck 1977; Greenberg 1978; Hong & Greenberg 1980; Draine & Lee 1984; Duley, Jones, & Williams 1989; Mathis & Whiffen 1989; Kim, Martin, & Hendry 1994; Mathis 1996; Li & Greenberg 1997; Zubko 1999; Weingartner & Draine 2001a). The near-IR (1–5 μ m), mid-IR (5–12 μ m) emission spectrum along with the far-IR (>12 μ m) continuum emission of the diffuse Galactic medium yields further insights into the composition and physical nature of interstellar dust; in particular, the PAH emission features allow us to place new constraints on the size distribution of the very small dust component.

To model this IR emission, we require realistic calculations of the excitation and deexcitation rates of small grains subject to stochastic heating by absorption of starlight, and cooling by spontaneous emission of infrared photons. We require detailed knowledge of the optical and thermal properties of interstellar dust materials to derive the probability distribution for the vibrational energy of a grain of specified size and composition.

Attempts to model the IR emission of interstellar dust have been made by various previous workers. Following the initial detection of 60 and 100 μ m cirrus emission (Low et al. 1984), Draine & Anderson (1985) calculated the IR emission from a graphite/silicate grain model with grains as small as 3 \AA and argued that the 60 and 100 μ m emission could be accounted for. When further processing of the IRAS data revealed stronger-than-expected 12 and 25 μ m emission from interstellar clouds (Boulanger, Baud, & van Albada 1985), Weiland et al. (1986) showed that this emission could be explained if very large numbers of 3–10 \AA grains were present. A step forward was taken by Désert, Boulanger, & Puget (1990), Siebenmorgen & Krügel (1992), Schutte, Tielens, & Allamandola (1993), and Dwek et al. (1997) by including PAHs as an essential grain component. Early studies were limited to the IRAS observation in four broad photometric bands, but Dwek et al. (1997) were able to use DIRBE and FIRAS data. No calculations have been carried out to ascertain whether *both* the PAH features *and* the far-IR continuum can be quantitatively reproduced.

There has been considerable progress in both experimental measurements and quantum chemical calculations of the optical properties of PAHs (Allamandola, Hudgins, & Sandford 1999a; Langhoff 1996; and references therein). There is also an improved understanding of the heat capacities of dust candidate materials (Draine & Li 2001a, hereafter DL01) and the stochastic heating of very small grains (Barker & Cherchneff 1989; d’Hendecourt et al. 1989; DL01) the interstellar dust size distributions (Weingartner & Draine 2001a, hereafter WD01a), and the grain charging processes (Weingartner & Draine 2001b). In the present paper we make use of these advances to model the full emission spectrum, from near-IR to submillimeter, of dust in the diffuse interstellar medium (ISM). The model is compared to IRTS, DIRBE, and FIRAS observations. We consider dust in three distinct regions: high-latitude regions ($|b| \gtrsim 25^\circ$; hereafter HGL); and two regions in the Galactic plane – the “MIRS” region ($44^\circ \leq l \leq 44^\circ 40'$, $-0^\circ 40' \leq b \leq 0^\circ$) for which the 4.5–11.7 μ m spectrum was obtained by the mid-IR spectrometer on board IRTS; and the “NIRS” region ($47^\circ 30' \leq l \leq 48^\circ$, $|b| \leq 15'$) for which the 2.8–3.9 μ m spectrum was obtained by the near-IR spectrometer on board IRTS.

In the present work we consider a dust model which is a natural extension of the original graphite-silicate model for interstellar dust (Mathis, Rumpl, & Nordsieck 1977; Draine & Lee 1984, hereafter DL84). Our dust model consists of two grain types – amorphous silicate grains and carbonaceous grains – both with size distributions ranging from ultrasmall grains/large molecules a few angstroms in size (in the molecular domain) to large grains $\gtrsim 1\mu\text{m}$ in diameter¹. We assume that the carbonaceous grains have graphitic properties at large sizes and PAH-like properties at very small sizes. For PAH-like grains, we distinguish between the optical properties of neutral PAHs and PAH ions. The current work assumes spherical grains and therefore does not yet address issues related to polarization.

This paper is organized as follows. We first explore in §2 the optical properties of interstellar dust materials, with emphasis on the absorption cross sections of both ionized and neutral PAHs from far-UV to far-IR. We then briefly summarize the heat capacities of PAHs, graphite and silicates in §3. In §4 we describe the radiation field adopted for the diffuse ISM. We calculate in §5 the equilibrium temperatures for large grains ($\gtrsim 200\text{\AA}$). In §6 we describe the methods developed in DL01 to calculate the energy distribution functions for very small ($a \lesssim 200\text{\AA}$) grains heated by starlight. Selected results are presented for illustration, and we demonstrate the importance of stochastic heating for grains as large as $a = 200\text{\AA}$.

The adopted dust size distribution functions are summarized in §7. The PAH charging computation is described in §8, and §9 details the IR emission modelling.

In §10 we discuss our choices of model parameters, and compare our model with observations of infrared emission from high galactic latitudes as well as two galactic plane regions. We find our model to be in very good agreement with observations from the near-IR (including the PAH emission features) to the submillimeter. We compute emission spectra for our “standard” dust heated by starlight with intensities ranging from 0.3 to 10^4 times the local value, and we tabulate the predicted intensities averaged over the SIRTf IRAC and MIPS photometric bands. The total infrared emission from our grain model is seen to be in excellent agreement with DIRBE observations, just as the albedo for our grain model is in accord with observations of the diffuse galactic light.

In §11 we show the extinction curve for our model, from the far-UV to submillimeter wavelengths, as well as tabulated values of the dust opacity. We discuss the elemental depletion, the aromatic absorption features, and the variations of the relative abundance of PAH in various regions. We also summarize the upper limits for the abundance of ultrasmall silicate grains (both amorphous and crystalline) estimated in Li & Draine (2001). Finally, we summarize our conclusions in §12.

2. Optical Properties of Interstellar Dust Materials

To calculate the energy (temperature) distribution functions of very small grains (undergoing “temperature fluctuations”), or the “equilibrium temperatures” of larger “classical” grains, and the resulting IR emission spectrum, an accurate knowledge of the absorption and emission properties of interstellar dust materials over a broad range of wavelengths is required.

¹To avoid confusion, we emphasize here that “very small grains”, “large molecules”, and “ultrasmall grains” are synonymous.

2.1. Silicate Grains

We use Mie theory (see, e.g., Bohren & Huffman 1983) to calculate the absorption and scattering cross sections for amorphous silicate spheres. We adopt the dielectric functions of DL84 with two modifications: 1) the sudden steep rise of the imaginary part in the far-UV has been smoothed (see WD01a); and 2) the dielectric function has been modified at $\lambda > 250\mu\text{m}$ to better match the average high Galactic latitude dust emission spectrum measured by FIRAS (Wright et al. 1991; Reach et al. 1995; Finkbeiner, Davis, & Schlegel 1999) – for $\lambda > 250\mu\text{m}$ we take the imaginary part of the silicate dielectric function to be

$$\epsilon_2(\lambda) = \epsilon_2^{\text{DL}}(\lambda) \times \begin{cases} \left[1 + \beta \frac{\ln(\lambda/250\mu\text{m}) \times \ln(\lambda/850\mu\text{m})}{\ln(850/250)} \right], & 250 \leq \lambda \leq 850\mu\text{m}, \\ (\lambda/850\mu\text{m})^\beta, & 850 \leq \lambda \leq 10^4\mu\text{m}, \\ (10^4/850)^\beta, & \lambda \geq 10^4\mu\text{m}. \end{cases} \quad (1)$$

where $\beta=0.4$, and ϵ_2^{DL} is the imaginary part of the DL84 silicate dielectric function. Using the Kramers-Kronig relation (see DL84), we have recomputed the real part of the silicate dielectric function from the newly modified ϵ_2 . The modification to $\epsilon_2(\lambda)$ and the absorption cross sections $C_{\text{abs}}(\lambda)$ for silicates is very slight except at very long wavelengths: there is no change at all for $\lambda \leq 250\mu\text{m}$, and for $250 < \lambda \leq 1100\mu\text{m}$ the new ϵ_2 is within $\pm 12\%$ of ϵ_2^{DL} . Only for $\lambda > 4.8\text{ mm}$ is the silicate emissivity altered by more than a factor of 2.

We stress that we do *not* intend to suggest that the dielectric function for “astronomical silicate” has been determined with the precision that might be suggested by the modest adjustments represented by eq. (1) – i.e., we do *not* believe that ϵ_2 is known to an accuracy of $\pm 12\%$ for $\lambda < 1100\mu\text{m}$. Our objective is simply to demonstrate that with an entirely reasonable dielectric function, our carbon-silicate grain model can accurately reproduce the available observations of the far-infrared emission spectrum. The original DL84 astro-silicate had $C_{\text{abs}} \propto \lambda^{-2.0}$ for $\lambda \gtrsim 100\mu\text{m}$. The above modification has $C_{\text{abs}} \propto \lambda^{-1.6}$ for $800 \lesssim \lambda < 1\text{ cm}$, similar to the $\lambda^{-1.6}$ frequency dependence observed by Agladze et al. (1996) over 700–2500 μm for amorphous 2MgO·SiO₂ grains at $T = 20\text{ K}$ [although note that at $\lambda = 1000\mu\text{m}$ we have a silicate opacity $\kappa = C_{\text{abs}}/(4\pi\rho a^3/3) = 0.33\text{ cm}^2\text{ g}^{-1}$, whereas the material studied by Agladze et al. (1996) had $\kappa = 1.25\text{ cm}^2\text{ g}^{-1}$ at this frequency].

2.2. Carbonaceous Grains

We assume a continuous distribution for the optical properties of interstellar carbonaceous grains with graphite-like properties for large sizes ($\gtrsim 50\text{Å}$) and PAH-like properties in the small size limit ($\lesssim 20\text{Å}$). The absorption cross sections $C_{\text{abs}}^{\text{gra}}(a, \lambda)$ of graphite grains are calculated from Mie theory using the “1/3–2/3 approximation” (Draine & Malhotra 1993) and the graphite dielectric functions of DL84. The absorption cross sections of PAHs will be discussed below (§2.3). Finally, we make a transition from PAH optical properties to graphite properties at $a = 50\text{Å}$ by taking the absorption cross sections of carbonaceous grains to be

$$C_{\text{abs}}^{\text{carb}}(a, \lambda) = \xi_{\text{PAH}} C_{\text{abs}}^{\text{PAH}}(a, \lambda) + (1 - \xi_{\text{PAH}}) C_{\text{abs}}^{\text{gra}}(a, \lambda) \quad (2)$$

$$\xi_{\text{PAH}}(a) = (1 - q_{\text{gra}}) \times \min [1, (a_\xi/a)^3], \quad a_\xi = 50\text{Å}, \quad q_{\text{gra}} = 0.01 \quad (3)$$

where $C_{\text{abs}}^{\text{PAH}}$, $C_{\text{abs}}^{\text{gra}}$ are, respectively, the absorption cross sections of PAHs and graphite grains of radius² a at wavelength λ ; a_ξ is the grain radius where the transition from PAH properties to graphite properties begins; $0 < q_{\text{gra}} \ll 1$ so that even for small carbonaceous grains we introduce a small amount of “continuum” absorption (see §2.3 below); ξ_{PAH} , the PAH “weight”, drops from $1 - q_{\text{gra}}$ to 0 as a increases from a_ξ to infinity. Our choice of the functional form of ξ_{PAH} is quite arbitrary, but the resultant IR spectrum is insensitive to the detailed behavior of ξ_{PAH} provided $\xi_{\text{PAH}} = (1 - q_{\text{gra}})$ for $a \lesssim 30\text{\AA}$ and $\xi_{\text{PAH}} \lesssim 0.5$ for $a \gtrsim 100\text{\AA}$. For example, the much flatter function, $\xi_{\text{PAH}}(a) = (1 - q_{\text{gra}}) \times \min\{1, 1/[1 + (a/a_\xi - 1)^3]\}$, results in a model spectrum (not shown here) which is nearly indistinguishable from that of eq.(3).

2.3. Absorption Cross Sections of PAHs

In the present model, a PAH molecule is characterized by the number of carbon atoms (N_C), the hydrogen to carbon ratio (H/C), and charge state (neutral or charged). The H/C ratio is determined by the aromatic structure. Since it seems likely that astronomical PAHs are relatively pericondensed, as favoured by stability considerations (van der Zwet & Allamandola 1985; Omont 1986; Allamandola et al. 1989; Jochims et al. 1994) and the fact that large compact PAHs provide a better match to interstellar PAH band positions (Langhoff 1996), we assume

$$\text{H/C} = \begin{cases} 0.5, & N_C \leq 25, \\ 0.5/\sqrt{N_C/25}, & 25 \leq N_C \leq 100, \\ 0.25, & N_C \geq 100, \end{cases} \quad (4)$$

which for $N_C < 100$ approximates those of compact, symmetric PAHs (series 1, 3 in Stein & Brown 1991). But we have also considered a higher H/C ratio which is appropriate for PAHs with more open, uneven structures (see §10.6).

Following previous workers (Léger, d’Hendecourt, & Défourneau 1989a; Désert et al. 1990; Schutte et al. 1993), we construct the absorption cross sections for both neutral and ionized PAHs from far-UV to far-IR based on available laboratory measurements and guided by the astronomical observations (see Appendix A for details). The resulting cross sections are characterized by a set of Drude profiles: the σ - σ^* transition with a peak at $\lambda_0^{-1} \simeq 14\mu\text{m}^{-1}$; the π - π^* transition with $\lambda_0^{-1} \simeq 4.6\mu\text{m}^{-1}$; the C-H stretching mode ($\lambda_0 = 3.3\mu\text{m}$); two C-C stretching modes ($\lambda_0 = 6.2, 7.7\mu\text{m}$); the C-H in-plane bending mode ($\lambda_0 = 8.6\mu\text{m}$); three C-H out-of-plane bending modes ($\lambda_0 = 11.3, 11.9, 12.7\mu\text{m}$); and a few weak features probably due to C-C bending modes ($\lambda_0 = 16.4, 18.3, 21.2, 23.1\mu\text{m}$). In addition to these discrete features, there is also far-UV, near-UV/visible and far-IR continuum absorption.

The absorption cross section per C atom $C_{\text{abs}}^{\text{PAH}}/N_C$ is taken to be

$$\frac{C_{\text{abs}}^{\text{PAH}}(\lambda)}{N_C} = C_{\text{abs}}^{\text{gra}}(\lambda)/N_C \quad x > 17.25; \quad (5)$$

$$= (126.0 - 6.4943x) \times 10^{-18} \text{ cm}^2/\text{C}, \quad 15 < x < 17.25; \quad (6)$$

$$= S_1(\lambda) + (-3.0 + 1.35x) \times 10^{-18} \text{ cm}^2/\text{C}, \quad 10 < x < 15; \quad (7)$$

$$= (66.302 - 24.367x + 2.950x^2 - 0.1057x^3) \times 10^{-18} \text{ cm}^2/\text{C}, \quad 7.7 < x < 10; \quad (8)$$

²We adopt a mass density $\approx 2.24 \text{ g cm}^{-3}$ for graphite. The “radius” a of a PAH containing N_C C atoms is *defined* to be the radius of a sphere with the carbon density of graphite containing the same number of C atoms, i.e., $a = 1.286N_C^{1/3} \text{\AA}$.

$$= S_2(\lambda) + \left[1.8687 + 0.1905x + 0.4175(x - 5.9)^2 + 0.04370(x - 5.9)^3 \right] \times 10^{-18} \text{ cm}^2/\text{C}, \quad 5.9 < x < 7.7; \quad (9)$$

$$= S_2(\lambda) + (1.8687 + 0.1905x) \times 10^{-18} \text{ cm}^2/\text{C}, \quad 3.3 < x < 5.9; \quad (10)$$

$$= 34.58 \times 10^{-18-3.431/x} \times \text{cutoff}(\lambda, \lambda_c) \text{ cm}^2/\text{C} + \sum_{j=3}^{14} S_j(\lambda), \quad x < 3.3; \quad (11)$$

where $x \equiv (\lambda/\mu\text{m})^{-1}$. The ultraviolet $\sigma\text{-}\sigma^*$ and $\pi\text{-}\pi^*$ transitions ($j=1,2$), C-H stretching ($j=3$), C-C stretching ($j=4,5$), C-H in-plane bending ($j=6$), C-H out-of-plane bending ($j=7,8,9$), C-C bending ($j=10,11,12,13$) modes, and far-IR continuum ($j=14$) are represented by Drude profiles, with the absorption cross section per carbon atom contributed by feature j given by

$$S_j(\lambda) \equiv \frac{2}{\pi} \frac{\gamma_j \lambda_j \sigma_{\text{int},j}}{(\lambda/\lambda_j - \lambda_j/\lambda)^2 + \gamma_j^2}, \quad (12)$$

where Table 1 lists values of the central wavelength λ_j , the broadening parameter γ_j , and the integrated absorption strength³

$$\sigma_{\text{int},j} \equiv \int S_j(\lambda) d\lambda^{-1} = \frac{\pi}{2} S_j(\lambda_j) \gamma_j \lambda_j^{-1}. \quad (13)$$

The function $\text{cutoff}(\lambda, \lambda_c)$ and the cutoff wavelength λ_c , determined by the PAH size (the number of fused benzenoid rings), are defined in eqs. (A2,A3).

Figure 1 plots the absorption spectrum of PAHs in the UV/far-UV. Also plotted are the experimental spectra of coronene ($\text{C}_{24}\text{H}_{12}$) (Léger et al. 1989b), PAH mixtures (Léger et al. 1989b; Joblin, Léger, & Martin 1992), and the cross section estimated for graphite (DL84). Figure 2 displays the absorption cross sections of neutral and ionized PAHs for a wide wavelength range with emphasis on the C-H, C-C IR vibrational modes (see following and §2.4, §A.3, §A.4 for details).

We have included enhancement factors $E_{6.2}$, $E_{7.7}$, and $E_{8.6}$ in the strengths of the 6.2, 7.7, and 8.6 μm bands⁴. For $E_{6.2} = E_{7.7} = E_{8.6} = 1$ we recover the laboratory values, but we are unable to satisfactorily reproduce astronomical spectra unless we take $E_{6.2}$, $E_{7.7}$, $E_{8.6} > 1$. For the 7.7 and 11.3 μm features, laboratory data (see §A.3) indicate a relative band strength $\sigma_{\text{int},7.7}/\sigma_{\text{int},11.3} \approx 1.3$ for neutral PAHs, and ≈ 12 for ionized PAHs (assuming $\text{H}/\text{C} = 1/3$). Let $P(\lambda_j) \equiv \int I_\lambda d\lambda$ be the total power integrated over the profile of feature j . Values of $P(7.7\mu\text{m})/P(11.3\mu\text{m})$ as large as 11 are observed in some objects, such as compact HII regions (Roelfsema et al. 1996). DL01 have modelled the emission expected from PAHs in various radiation fields, and find that for $E_{7.7}=2$, fully ionized PAHs with $N_C < 100$ in a region of very intense UV radiation (up to $10^6 \times$ the Habing [1968] UV intensity) achieve $P(7.7\mu\text{m})/P(11.3\mu\text{m}) \approx 21$. However, since the observed spectra include emission from larger PAHs with smaller values of $P(7.7\mu\text{m})/P(11.3\mu\text{m})$, it is necessary to take $E_{7.7} \approx 2$ to reproduce the strength of the strongest observed 7.7 μm features.

In addition, a wide variety of objects show a $P(6.2\mu\text{m})/P(7.7\mu\text{m})$ ratio exceeding the maximum predicted from the laboratory PAH feature strengths. For example, $P(6.2\mu\text{m})/P(7.7\mu\text{m}) \approx 0.3 - 0.6$ in a

³The cross section integrated over wavelength $\int S_j(\lambda) d\lambda = \lambda_j^2 \sigma_{\text{int},j}$.

⁴Absolute band strengths for some PAH species vary considerably among different laboratory groups and between experimental results and theoretical calculations. For example, the integrated cross sections of naphthalene, anthracene, tetracene, phenanthrene, benzanthracene, pyrene, and coronene cations can differ by a factor of 1.5–20 between different experimental studies, or between experimental and theoretical studies (see Langhoff 1996).

Table 1: Drude profile parameters for model PAHs.

j	λ_j (μm)	λ_j^{-1} (cm^{-1})	γ_j	FWHM		$\sigma_{\text{int},j} \equiv \int S_j(\lambda) d\lambda^{-1}$	
				$\gamma_j \lambda_j$ (μm)	$\gamma_j \lambda_j^{-1}$ (cm^{-1})	neutral (10^{-20}cm/C)	ionized (10^{-20}cm/C)
1	.0722	138500	0.195	.0141	27000	7.97×10^7	7.97×10^7
2	.2175	46000	0.217	.0473	10000	1.23×10^7	1.23×10^7
3	3.3	3030	0.012	0.04	37	$197 \times \text{H/C}$	$44.7 \times \text{H/C}$
4 ^a	6.2	1610	0.032	0.20	52	$19.6 \times E_{6.2}$	$157 \times E_{6.2}$
5 ^a	7.7	1300	0.091	0.70	118	$60.9 \times E_{7.7}$	$548 \times E_{7.7}$
6 ^a	8.6	1161	0.047	0.40	54	$34.7 \times E_{8.6} \times \text{H/C}$	$242 \times E_{8.6} \times \text{H/C}$
7 ^b	11.3	886	0.018	0.20	16	$427 \times (1/3)\text{H/C}$	$400 \times (1/3)\text{H/C}$
8 ^b	11.9	840	0.025	0.30	21	$72.7 \times (1/3)\text{H/C}$	$61.4 \times (1/3)\text{H/C}$
9 ^b	12.7	787	0.024	0.30	19	$167 \times (1/3)\text{H/C}$	$149 \times (1/3)\text{H/C}$
10 ^c	16.4	610	0.010	0.16	6	5.52	5.52
11 ^d	18.3	546	0.036	0.66	20	6.04	6.04
12 ^d	21.2	472	0.038	0.81	18	10.8	10.8
13 ^d	23.1	433	0.046	1.07	20	2.78	2.78
14 ^e	26.0	385	0.69	18.0	266	15.2	15.2

^aWith $E_{6.2}=1$, $E_{7.7}=1$ and $E_{8.6}=1$ one obtains the laboratory measured band strengths. The observed IR spectrum of the diffuse ISM is best fitted by our dust model with $E_{6.2}=3$, $E_{7.7}=2$ and $E_{8.6}=2$.

^bFor the C-H out-of-plane bending modes, the $\frac{1}{3}$ factor arises from the assumption that PAHs have equal numbers of H in solo, duet, and trio adjacent CH units (see §A.3).

^cBand width from Moutou et al. (2000).

^dBand widths from Moutou et al. (1996).

^eTo reproduce the weak $\lambda > 14\mu\text{m}$ continuum absorption measured by Moutou et al. (1996).

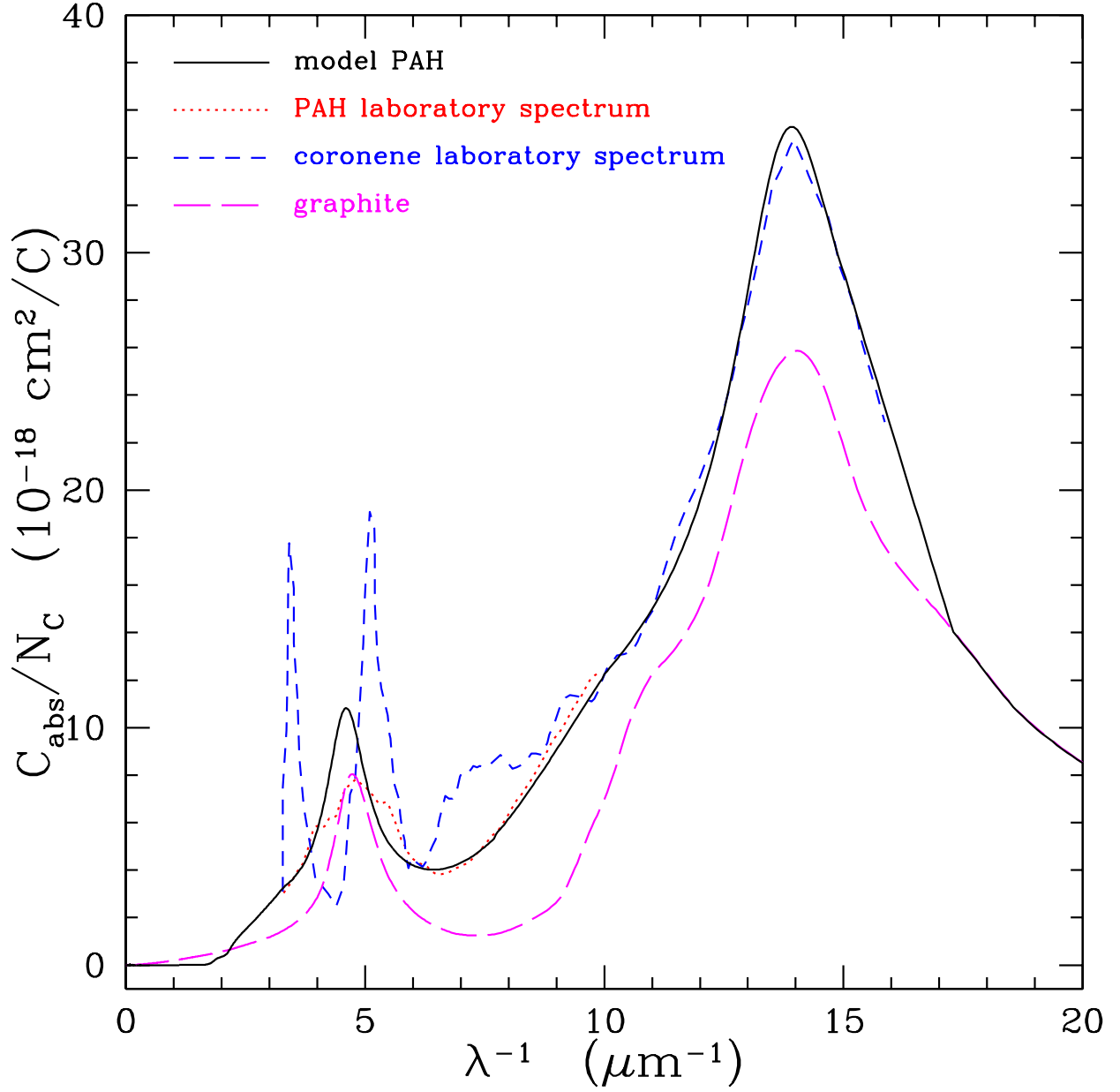


Fig. 1.— The ultraviolet and far ultraviolet absorption cross section per C atom of PAHs.

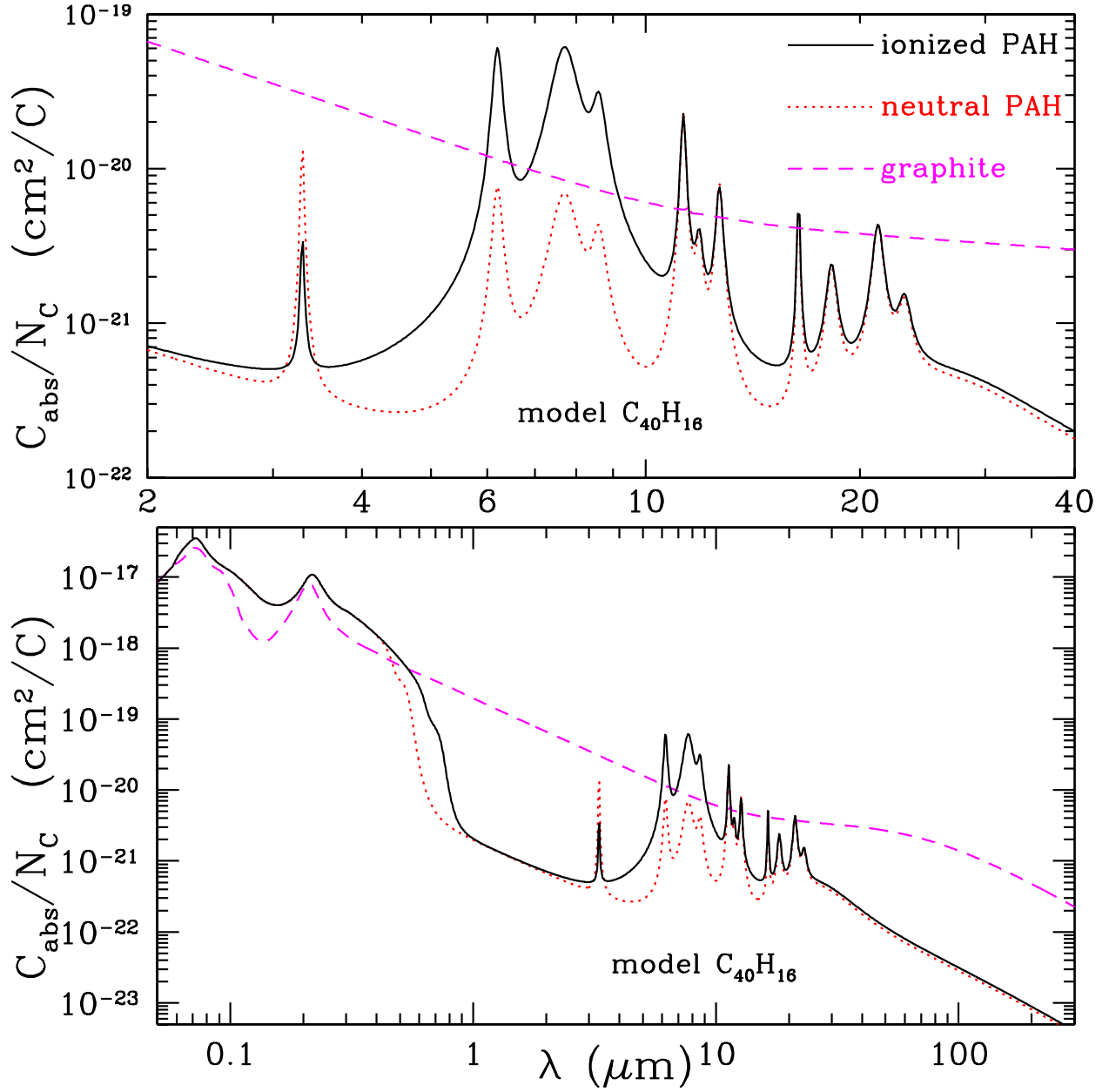


Fig. 2.— Absorption cross section per C atom of neutral and ionized PAHs (with $E_{6.2}=3$, $E_{7.7}=2$, $E_{8.6}=2$). Ionization enhances the C-C stretching modes (6.2, 7.7 μm) and C-H in-plane bending mode (8.6 μm), and weakens the C-H stretching mode (3.3 μm). Ionization shifts the visual absorption edge (which is also size-dependent) redward. The absorption cross section per C atom of small graphite spheres is shown for comparison.

recent study of 820 mid-IR spectra of the diffuse interstellar medium (Chan et al. 2001), and ≈ 0.54 for an average of planetary nebulae, reflection nebulae, and HII regions (Cohen et al. 1989). Thermal emission has a strict upper limit $P(6.2\mu\text{m})/P(7.7\mu\text{m}) < (7.7/6.2)^2 \sigma_{\text{int},6.2}/\sigma_{\text{int},7.7} \approx 0.44 E_{6.2}/E_{7.7}$ (see Table 1), and detailed modelling of stochastic heating finds $P(6.2\mu\text{m})/P(7.7\mu\text{m}) \lesssim 0.35 E_{6.2}/E_{7.7}$ (see Figure 16 in DL01). Therefore, we take $E_{6.2} = 1.5 E_{7.7} \approx 3$.

For most objects, the strength of the $8.6\mu\text{m}$ C-H in-plane bending mode is consistent with the strength of the $7.7\mu\text{m}$ C-C bending mode, so we take $E_{8.6} = E_{7.7} \approx 2$.

2.4. Continuum Opacity of Polycyclic Aromatic Hydrocarbons

Even when $a < a_\xi$, eqs. (2,3) cause C_{abs} to include a fraction q_{gra} of the opacity per C atom of graphite, resulting in “continuum” opacity extending into the infrared. This is required to account for the near-IR continuum emission at $1\text{--}5\mu\text{m}$ underlying the $3.3\mu\text{m}$ C-H stretching feature detected in a number of astronomical objects, including the Orion Bar (Joblin et al. 1996a; Bregman et al. 1989; Geballe et al. 1989), various reflection nebulae (Sellgren, Werner, & Allamandola 1996), the Red Rectangle (Geballe et al. 1989), normal galaxies (Helou et al. 2000), and the starburst galaxies M82 and NGC 253 (Sturm et al. 2000). This continuum emission may arise from the electronic fluorescence or a quasi-continuum of overlapping overtone and combination bands from vibrational fluorescence in PAHs (Léger & Puget 1984; Allamandola et al. 1985, 1989; Sellgren et al. 1996). Electronic intraband transitions can also contribute an optical-infrared continuum due to the closing of the band gap as the PAH size increases and/or upon ionization of the PAH (Allamandola et al. 1989; Tielens et al. 1999).

We represent this continuum by the parameter q_{gra} in eq. (3). High resolution spectroscopic observations of NGC 1333 (Joblin et al. 1996a), the Orion Bar (Geballe et al. 1989; Joblin et al. 1996a), and the Red Rectangle (Geballe et al. 1989) resolving the $3.3\mu\text{m}$ feature with $\text{FWHM} \approx 0.04\mu\text{m}$ (same as that adopted here) show a feature peak-to-continuum ratio as high as ~ 30 . If we require a $3.3\mu\text{m}$ peak-to-continuum ratio of 30, then PAHs with $N_{\text{C}} \lesssim 50$ (small enough to be heated to $T \gtrsim 1500\text{ K}$ by a UV photon – see DL01) must have

$$q_{\text{gra}} \approx \frac{1}{30} \times \frac{2 \times 3.3\mu\text{m} \times \sigma_{\text{int},3.3\mu\text{m}}}{\pi \gamma_{3.3} C_{\text{abs}}^{\text{gra}}(3.3\mu\text{m})} \approx 0.01, \quad (14)$$

where we have taken $C_{\text{abs}}^{\text{gra}}(3.3\mu\text{m}) \approx 3 \times 10^{-20} N_{\text{C}} \text{ cm}^2$, $\text{H/C} \approx 1/3$, and have taken $\sigma_{\text{int},3.3\mu\text{m}}$ to be the average of the values in Table 1 for neutral and ionized PAHs. The resulting PAH infrared cross sections are shown in Figure 2, for both neutral and ionized PAHs.

Finally, there is the question of the value of a_ξ . The observed PAH emission features are at $\lambda \lesssim 25\mu\text{m}$, and this will be contributed primarily by particles with $a \lesssim 40\text{ \AA}$ which can be heated to $\gtrsim 100\text{ K}$ by a photon with $hc/\lambda < 13.6\text{ eV}$. Therefore, the observed PAH emission features only require $a_\xi \gtrsim 25\text{ \AA}$. We will take $a_\xi \approx 50\text{ \AA}$ so that the $6.2\mu\text{m}$ feature in *absorption* is in agreement with observations, as discussed in §12, but this value – as well as the form of the transition from PAH-like to graphitic optical properties (§2.2) – is poorly determined, as the calculated emission spectrum is relatively insensitive to variations in a_ξ in the range $25\text{--}100\text{ \AA}$. IR spectra calculated with $a_\xi = 25\text{ \AA}$ or $a_\xi = 75\text{ \AA}$ (not shown here) are almost identical to that for $a_\xi = 50\text{ \AA}$.

3. Enthalpies

As discussed in DL01, the vibrational energy of a PAH molecule containing N_C C and $(H/C) \times N_C$ H atoms can be approximated as

$$E_{\text{PAH}}(T) = \frac{H}{C} N_C \sum_{j=1}^3 \frac{\hbar \omega_j}{\exp(\hbar \omega_j / kT) - 1} + (N_C - 2) [k \Theta_{op} f_2(T/\Theta_{op}) + 2k \Theta_{ip} f_2(T/\Theta_{ip})] \quad ; \quad (15)$$

the summation index $j = 1 - 3$ runs over the C-H out-of-plane bending ($\omega_1/2\pi c = 886 \text{ cm}^{-1}$), in-plane bending ($\omega_2/2\pi c = 1161 \text{ cm}^{-1}$), and stretching ($\omega_3/2\pi c = 3030 \text{ cm}^{-1}$) modes; the term containing $N_C - 2$ is a two-dimensional Debye model with Debye temperatures $\Theta_{op} \approx 863 \text{ K}$ for the out-of-plane C-C modes, $\Theta_{ip} \approx 2504 \text{ K}$ for the in-plane C-C modes; k is the Boltzman constant; T is the “vibrational temperature”; and

$$f_n(x) = \frac{1}{n} \int_0^1 \frac{y^n dy}{\exp(y/x) - 1}. \quad (16)$$

For graphitic grains, we use eq. (15) with $H/C = 0$ (see DL01).

For amorphous silicate grains, DL01 recommend

$$E_{\text{sil}}(T) = (N_{\text{atom}} - 2) [2k \Theta_2 f_2(T/\Theta_2) + k \Theta_3 f_3(T/\Theta_3)], \quad (17)$$

where N_{atom} is the number of atoms contained in the silicate grain (we assume a mass density 3.5 g cm^{-3} for MgFeSiO_4 silicate material); $\Theta_2 \approx 500 \text{ K}$, $\Theta_3 \approx 1500 \text{ K}$ are Debye temperatures for the two- and three-dimensional Debye models, respectively.

4. Radiation Field

We adopt the solar neighbourhood interstellar radiation field (ISRF) (Mathis, Mezger, & Panagia 1983; hereafter MMP) for the diffuse ISM

$$u_\lambda = \chi_{\text{MMP}} \left\{ u_\lambda^{\text{UV}\odot} + \sum_{i=2}^4 W_i \frac{4\pi}{c} B_\lambda(T_i) \right\} + \frac{4\pi}{c} B_\lambda(2.9\text{K}) \quad (18)$$

where χ_{MMP} describes the enhancement of the starlight component (relative to the solar neighborhood)⁵; $u_\lambda^{\text{UV}\odot}$ is the ultraviolet component; $(W_2, W_3, W_4) = (10^{-14}, 10^{-13}, 4 \times 10^{-13})$ and $(T_2, T_3, T_4) = (7500, 4000, 3000) \text{ K}$ are dilution factors and corresponding black-body temperatures. The last term is the cosmic background radiation.

5. Thermal Equilibrium Temperatures of Large Grains

Large grains maintain a nearly constant temperature \bar{T} determined by balancing absorption and emission,

$$\int_0^\infty C_{\text{abs}}(a, \lambda) c u_\lambda d\lambda = \int_0^\infty C_{\text{abs}}(a, \lambda) 4\pi B_\lambda(\bar{T}) d\lambda \quad , \quad (19)$$

⁵Note that $\chi_{\text{MMP}} = 1$ corresponds to $\chi = 1.23$, where χ is the ratio of the intensity relative to the Habing (1968) estimate at 1000\AA , or $G_0 = 1.14$, where G_0 is the 6–13.6 eV energy density relative to the 6–13.6 eV energy density in the Habing (1968) radiation field.

where $C_{\text{abs}}(a, \lambda)$ is the absorption cross section for a grain with size a at wavelength λ , c is the speed of light, $B_\lambda(T)$ is the Planck function at temperature T , and u_λ is the energy density of the radiation field (see §4). In Figure 3 we display these “equilibrium” temperatures for graphitic and silicate grains as a function of size in environments with various UV intensities.

6. Transient Heating of Very Small Grains

Since Greenberg (1968) first noted that very small grains heated by starlight would experience temperature spikes, there have been a number of theoretical studies of this process. DL01 have recently carried out a detailed study in which they compared the energy distribution functions and resulting emission spectra calculated “exactly” (the “*exact-statistical*” method) versus two approximations: the “*thermal-discrete*” approximation and the “*thermal-continuous*” approximation. The *exact-statistical* method involves calculation of the vibrational density of states. In contrast, both the *thermal-discrete* method and the *thermal-continuous* method assume that at any given time, the vibrationally excited grain has a “vibrational temperature”, and the deexcitation process is assumed to correspond to a thermal emission spectrum. In the *thermal-discrete* method both the excitation and deexcitation processes are treated as discrete events; however, in the *thermal-continuous* method, the deexcitation process is approximated as continuous rather than discrete.

Although the thermal methods are not exact, DL01 have shown that the overall IR emission spectrum calculated using the *thermal-discrete* and the *thermal-continuous* methods is very close to that of the exact treatment (see also Barker & Cherchneff 1989; d’Hendecourt et al. 1989; Allamandola et al. 1989; Schutte et al. 1993). Since the *exact-statistical* method involves heavy computations of the grain vibrational mode spectrum and density of states, we adopt the *thermal-discrete* method. Figures 4 and 5 show the energy distribution functions found for PAHs and silicate grains with radii $a = 5, 10, 25, 50, 75, 100, 150, 200, 300 \text{ \AA}$ illuminated by the average ISRF ($\chi_{\text{MMP}} = 1$). Very small grains ($a \lesssim 100 \text{ \AA}$) have a very broad $P(E)$, and the smallest grains ($a \lesssim 30 \text{ \AA}$) have an appreciable probability P_0 of being found in the vibrational ground state $E = 0$. As the grain size increases, $P(E)$ becomes narrower, so that for $\chi_{\text{MMP}} = 1$ it can be approximated by a delta function for $a > 250 \text{ \AA}$. However, for radii as large as $a = 200 \text{ \AA}$, both carbonaceous and silicate grains have energy distribution functions which are broad enough that the emission spectrum deviates noticeably from the emission spectrum for grains at a single temperature \bar{T} , as shown in Figure 6. For accurate computation of infrared emission spectra it is therefore important to properly calculate the energy distribution function $P(E)$, including grain sizes which are large enough that the average thermal energy content exceeds a few eV.

7. Grain Size Distributions

Following Weingartner & Draine (2001a), we adopt size distribution functions for silicate grains and carbonaceous grains of the following form:

$$\frac{1}{n_{\text{H}}} \frac{dn_{\text{sil}}}{da} = \frac{C_{\text{sil}}}{a} \left(\frac{a}{a_{\text{t,sil}}} \right)^{\alpha_{\text{sil}}} F(a; \beta_{\text{t,sil}}, a_{\text{t}}) \times G(a; a_{\text{t,sil}}, a_{\text{c,sil}}), \quad (20)$$

$$\frac{1}{n_{\text{H}}} \frac{dn_{\text{carb}}}{da} = D(a) + \frac{C_{\text{carb}}}{a} \left(\frac{a}{a_{\text{t,carb}}} \right)^{\alpha_{\text{carb}}} F(a; \beta_{\text{t,carb}}, a_{\text{t}}) \times G(a; a_{\text{t,carb}}, a_{\text{c,carb}}), \quad (21)$$

$$F(a; \beta, a_{\text{t}}) \equiv \begin{cases} 1 + \beta a/a_{\text{t}}, & \beta \geq 0 \\ 1/(1 - \beta a/a_{\text{t}}), & \beta < 0 \end{cases}, \quad (22)$$

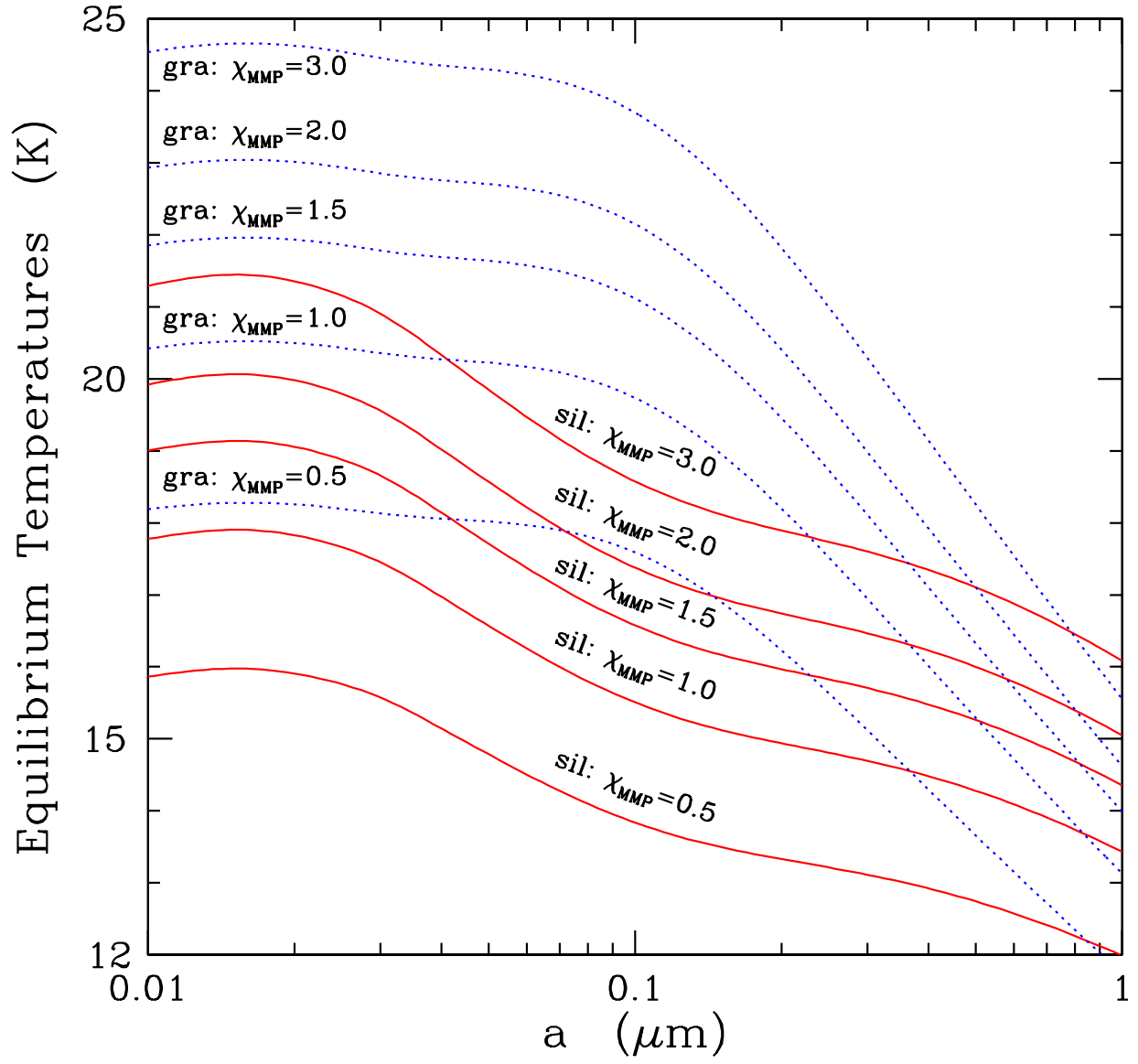


Fig. 3.— Equilibrium temperatures for graphite (dotted lines) and silicate grains (solid lines) in environments with various starlight intensities.

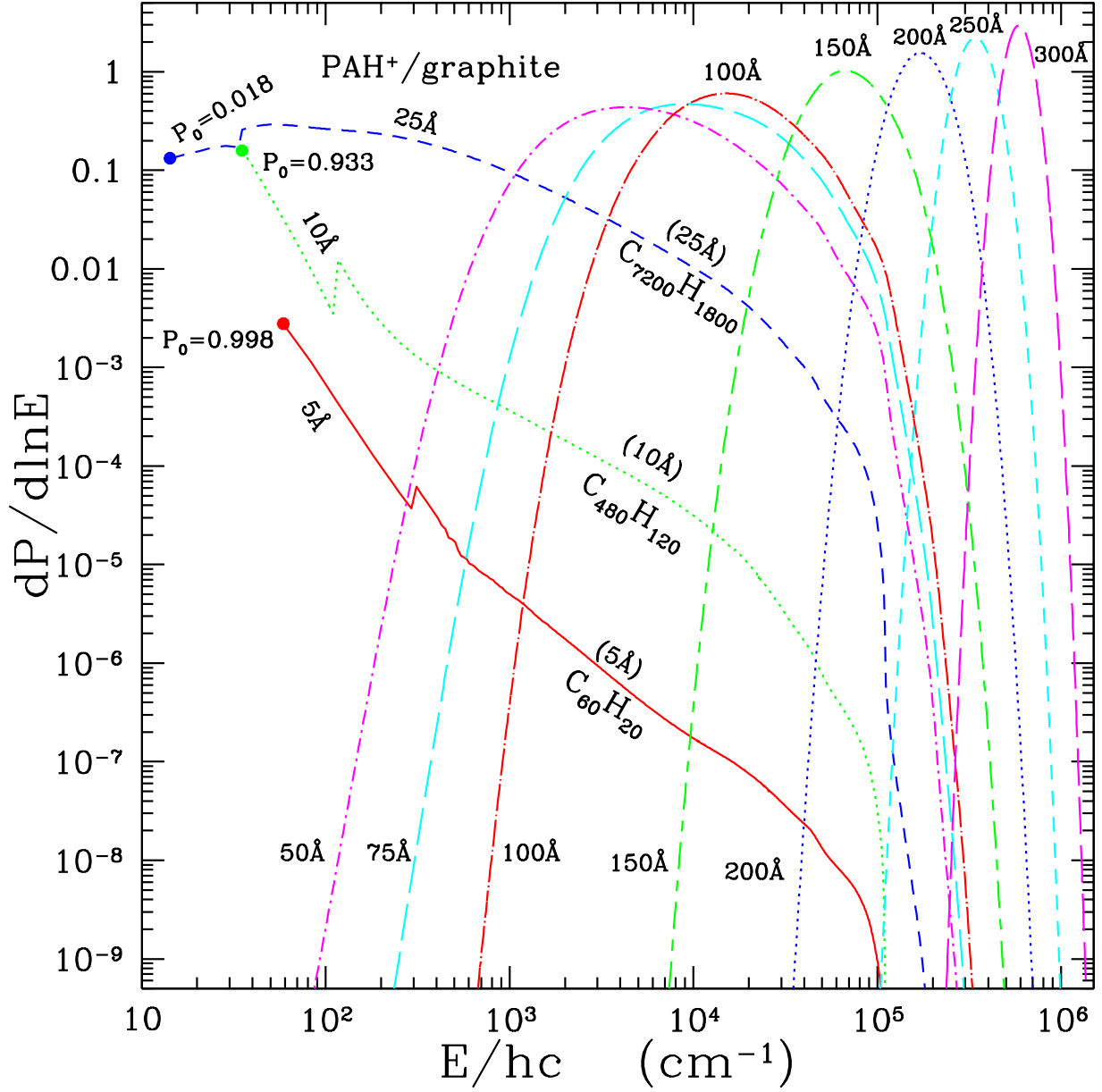


Fig. 4.— The energy distribution functions for charged carbonaceous grains ($a = 5$ [$\text{C}_{60}\text{H}_{20}$], 10 [$\text{C}_{480}\text{H}_{120}$], 25 [$\text{C}_{7200}\text{H}_{1800}$], 50 , 75 , 100 , 150 , 200 , 250 , 300\AA) for $\chi_{\text{MMP}} = 1$. The discontinuity in the 5 , 10 , and 25\AA curves is due to the change of the estimate for grain vibrational “temperature” at the 20th vibrational mode (see DL01). For 5 , 10 , and 25\AA a dot indicates the first excited state, and P_0 is the probability of being in the ground state.

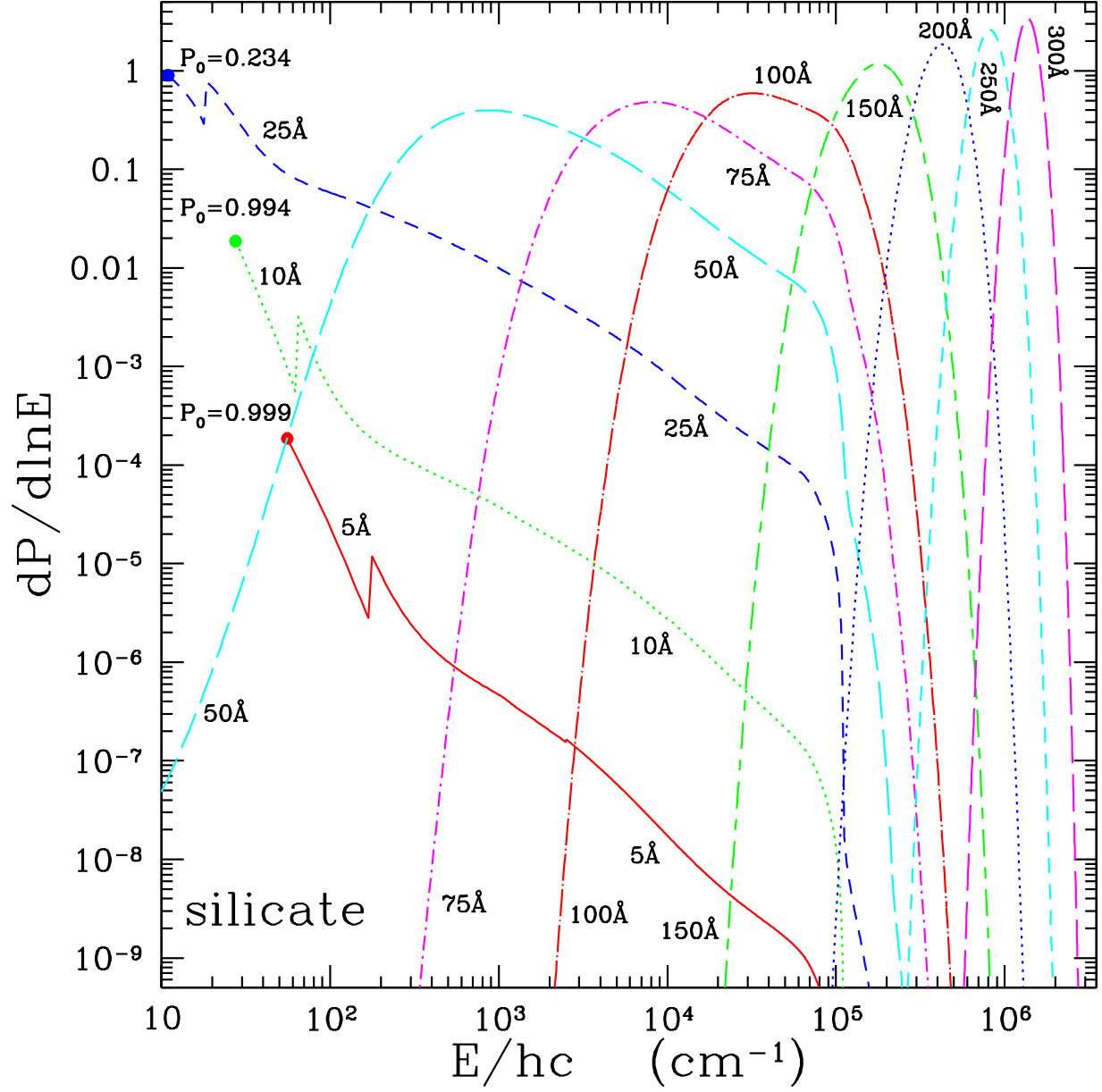


Fig. 5.— As in Figure 4, but for silicate grains.

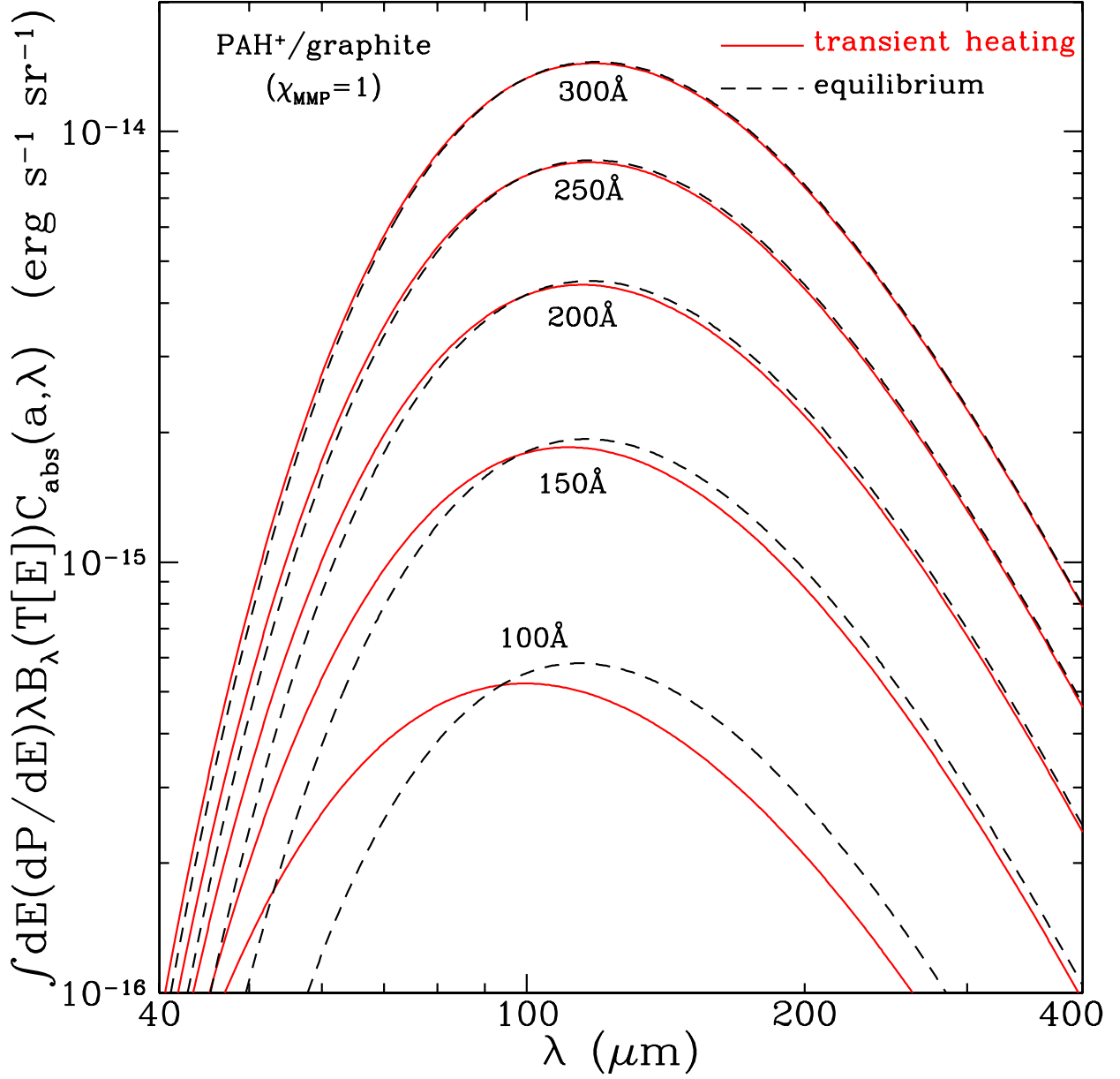


Fig. 6.— Infrared emission spectra for small carbonaceous grains of various sizes heated by starlight with $\chi_{\text{MMP}} = 1$, calculated using the full energy distribution function $P(E)$ (solid lines); also shown (broken lines) are spectra computed for grains at the “equilibrium” temperature \bar{T} . Transient heating effects lead to significantly more short wavelength emission for $a \lesssim 200 \text{ \AA}$.

$$G(a; a_t, a_c) \equiv \begin{cases} 1, & 3.5 \text{ \AA} < a < a_t \\ \exp \{ -[(a - a_t)/a_c]^3 \}, & a > a_t \end{cases}, \quad (23)$$

where n_H is the hydrogen number density, and $D(a)$ is an additional population of very small ($a \lesssim 100 \text{ \AA}$) carbonaceous grains which is introduced in order for the grain model to reproduce the observed infrared emission. The grains in the distribution $D(a)$ are all in the Rayleigh limit at the wavelengths $\lambda > 1000 \text{ \AA}$ where interstellar extinction has been measured, and therefore extinction measurements constrain only b_C , the number of carbon atoms per total H atoms in the population $D(a)$. For the PAH ultraviolet absorption cross section discussed in §2.3, WD01a showed that values of $b_C \leq 60\text{ppm}$ are allowed for the average diffuse ISM extinction law ($R_V = 3.1$). For a given choice of b_C within the allowed range, the parameters $a_{t,\text{sil}}$, $a_{c,\text{sil}}$, α_{sil} , β_{sil} , C_{sil} , $a_{t,\text{carb}}$, $a_{c,\text{carb}}$, α_{carb} , β_{carb} , C_{carb} can be found in WD01a.

The population of very small grains required to explain the IR emission of the cirrus and translucent molecular clouds is larger than could be obtained from simple extrapolation of the MRN power law ($dn/da \propto a^{-3.5}$) to very small sizes (Weiland et al. 1986; Désert et al. 1990; Dwek et al. 1997; Verter et al. 2000), and therefore $D(a)$ must include such very small grains. The observed infrared emission requires a substantial population of grains in the $5 - 10 \text{ \AA}$ size range so that single-photon heating can raise them to high enough temperatures to emit in the $3 - 12 \mu\text{m}$ range (see DL01). A log-normal distribution was used by Draine & Lazarian (1998) to represent the size distribution of ultrasmall carbonaceous grains producing both $3 - 12 \mu\text{m}$ infrared vibrational emission and microwave rotational emission, and we adopt such a distribution here.

We will see below (see Figure 8) that the $a \gtrsim 100 \text{ \AA}$ grains in the present grain model, with the adopted optical properties of graphite and silicate grains, produce less emission than observed near $60 \mu\text{m}$ for $a \gtrsim 100 \text{ \AA}$ grains, as the steady-state grain temperatures \bar{T} are slightly too cool. This could be because the grain properties may be in error – perhaps C_{abs} is too low in the optical and ultraviolet, or too large in the far-IR, or perhaps the starlight radiation field has been underestimated. However, we find that the grain model gives excellent agreement with the total radiated power (suggesting that the product of starlight intensity and optical-UV absorption cross sections are about right), and excellent agreement with the $\lambda \gtrsim 100 \mu\text{m}$ emission (suggesting that the far-IR emission cross sections are about right).

As previously suggested by Draine & Anderson (1985), the shortfall at $60 \mu\text{m}$ could be made up by emission from a population of very small grains which single-photon heating can raise to $\sim 40 \text{ K}$, so that much of the absorbed energy will be radiated near $60 \mu\text{m}$. The optimal grain size for this purpose is $a \approx 50 \text{ \AA}$. We use a second log-normal component to add a population of $a \approx 50 \text{ \AA}$ grains to $D(a)$:

$$D(a) = \sum_{i=1}^2 \frac{B_i}{a} \exp \left\{ -\frac{1}{2} \left[\frac{\ln(a/a_{0i})}{\sigma} \right]^2 \right\}, \quad a > 3.5 \text{ \AA} \quad (24)$$

$$B_i = \frac{3}{(2\pi)^{3/2}} \frac{\exp(-4.5\sigma^2)}{a_{0i}^3 \rho \sigma} \frac{m_C b_{C,i}}{\{1 + \text{erf}[3\sigma/\sqrt{2} + \ln(a_{0i}/3.5 \text{ \AA})/\sigma\sqrt{2}]\}} \quad , \quad \sum_{i=1}^2 b_{C,i} = b_C, \quad (25)$$

where m_C is the mass of a C atom; $\rho = 2.24 \text{ g cm}^{-3}$ is the mass density of graphite; a_{0i} determines the location of the peak, $b_{C,i}$ is the amount of C atoms relative to H consumed by the i -th log-normal component. The width of each of the log-normal components is determined by σ . The lower cutoff is set at $a=3.5 \text{ \AA}$ (corresponding to $N_C \approx 20$ for PAHs) since smaller grains are photolytically unstable (Omout 1986; Allamandola et al. 1989; Guhathakurta & Draine 1989). Component i of $D(a)$ has $a^3 dn/d \ln a$ peaking at $a_{\text{peak},i} = a_{0i} \exp(3\sigma^2)$.

As we will show below, we obtain a good fit to the observed interstellar emission spectrum with $b_{C1} = 45\text{ppm}$, $a_{01} = 3.5 \text{ \AA}$, $b_{C2} = 15\text{ppm}$, $a_{02} = 30 \text{ \AA}$, and $\sigma = 0.4$. The resulting size distribution, with $a^3 dn/d \ln a$

having three separate peaks at $\sim 6 \text{ \AA}$, $\sim 50 \text{ \AA}$, and 3000 \AA (see Figure 2 of WD01a) seems somewhat artificial, but this may be attributable in part to the procedure used for fitting the UV extinction.

8. PAH Charging

Due to their low ionization potential (6–7 eV), PAH molecules can be ionized through photoelectric emission (Allamandola et al. 1985; van der Zwet & Allamandola 1985; Lepp & Dalgarno 1988; Bakes & Tielens 1994). On the other hand, PAHs may also acquire charge through collisions with electrons and ions (Draine & Sutin 1987). The grain charging process has been recently reanalyzed by Weingartner & Draine (2001b); we use their rates for photoelectric emission and electron capture to study PAH charging in three idealized interstellar environments characterizing the diffuse ISM: cold neutral medium (CNM), warm neutral medium (WNM), and warm ionized medium (WIM). The parameters adopted in the PAH charge distribution computation are displayed in Table 2.

We estimate $\phi_{\text{ion}}(a)$ – the probability of finding a PAH molecule of radius a in a non-zero charge state – for CNM, WNM, and WIM respectively. In Figure 5 we present the PAH “ionization fraction” $\phi_{\text{ion}}(a)$ as a function of size for CNM, WNM, and WIM conditions, and in addition the average $\phi_{\text{ion}}(a)$ for the mass fractions listed in Table 2.

9. Modeling the IR Emission Spectrum

With the absorption cross sections $C_{\text{abs}}(a, \lambda)$ (§2), the UV radiation field strength χ_{MMP} (§4), the grain size distribution (§7), the energy distribution functions $P(E)$ for very small grains (§6), the equilibrium temperature \bar{T} for large grains (§5), and the ionization fraction $\phi_{\text{ion}}(a)$ of PAHs (§8), we can now calculate the IR emission spectrum from a mixture of silicate and carbonaceous grains. The IR emissivity per H nucleon, for dust illuminated by starlight of strength χ , is

$$\begin{aligned}
 E_{\lambda}(\chi) = & \left\{ \int_{250 \text{ \AA}}^{a_{\text{sil}}^{\text{max}}} da \frac{1}{n_{\text{H}}} \frac{dn_{\text{sil}}}{da} C_{\text{abs}}^{\text{sil}}(a, \lambda) B_{\lambda}(\bar{T}_{\text{sil}}[a, \chi]) \right. \\
 & + \int_{250 \text{ \AA}}^{a_{\text{carb}}^{\text{max}}} da \frac{1}{n_{\text{H}}} \frac{dn_{\text{carb}}}{da} C_{\text{abs}}^{\text{carb}}(a, \lambda) B_{\lambda}(\bar{T}_{\text{carb}}[a, \chi]) \\
 & + \int_{a_{\text{min}}}^{250 \text{ \AA}} da \frac{1}{n_{\text{H}}} \frac{dn_{\text{sil}}}{da} \int_{hc/\lambda}^{\infty} dE \left(\frac{dP}{dE} \right)_{\text{sil}} C_{\text{abs}}^{\text{sil}}(a, \lambda) B_{\lambda}(T_{\text{sil}}[E, a]) \\
 & \left. + \int_{a_{\text{min}}}^{250 \text{ \AA}} da \frac{1}{n_{\text{H}}} \frac{dn_{\text{carb}}}{da} \int_{hc/\lambda}^{\infty} dE \left[\phi_{\text{ion}} \left(\frac{dP}{dE} \right)_{\text{carb}^+} C_{\text{abs}}^{\text{carb}^+}(a, \lambda) B_{\lambda}(T_{\text{carb}^+}[E, a]) \right] \right\}
 \end{aligned}$$

Table 2: Idealized phases for the diffuse ISM .

Item	CNM	WNM	WIM
Mass fraction	0.43	0.43	0.14
$n_{\text{H}} (\text{cm}^{-3})$	30	0.4	0.1
$T (\text{K})$	100	6000	8000
$n_{\text{e}}/n_{\text{H}}$	0.0015	0.1	0.99

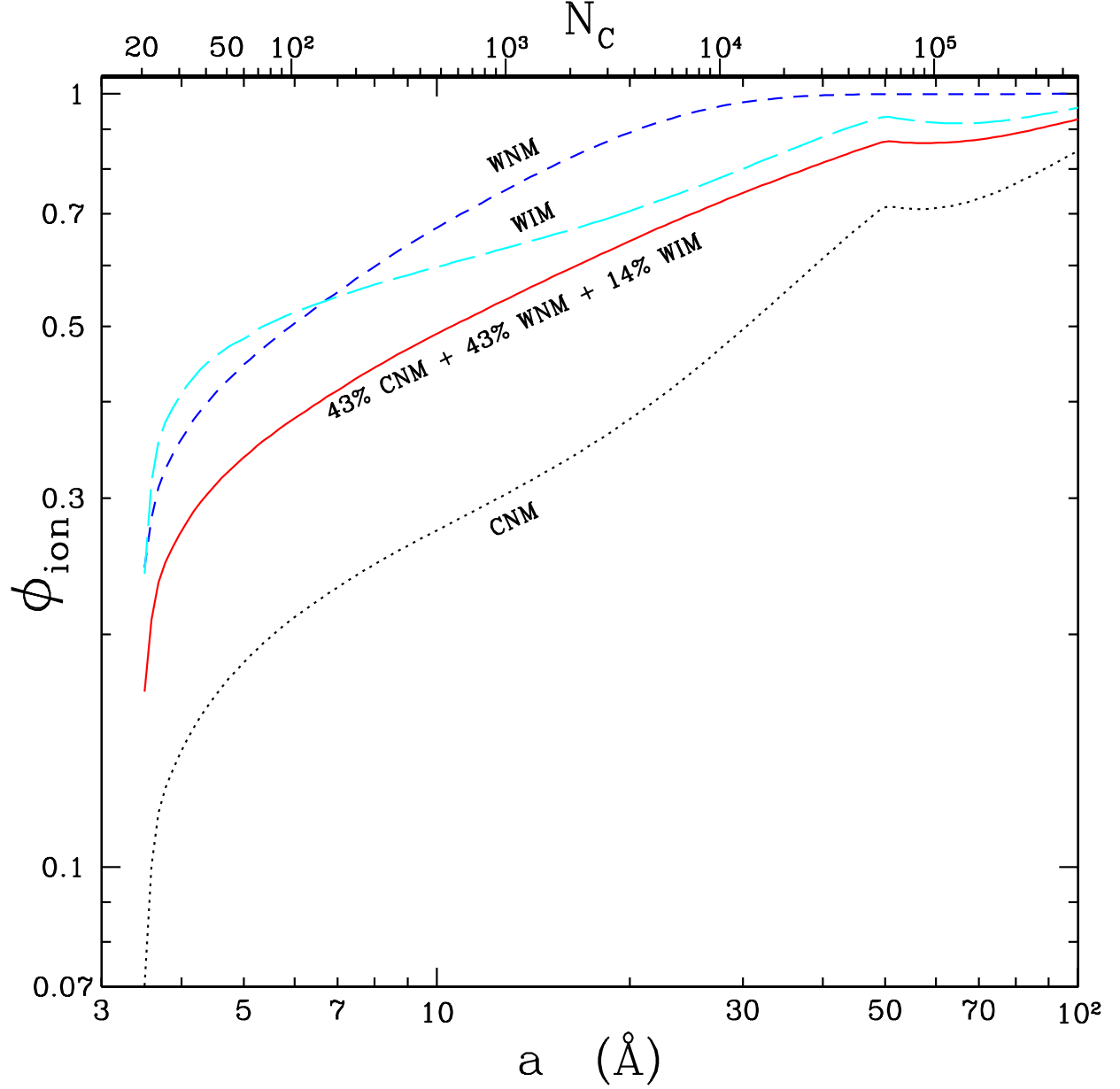


Fig. 7.— The “ionization fraction” ϕ_{ion} – the probability of finding a PAH molecule in a non-zero charge state – as a function of size for three idealized phases of the diffuse ISM: CNM (dotted), WNM (short-dashed), and WIM (long-dashed). Solid line shows the averaged ionization fraction weighted by the mass fractions of Table 2. The slope discontinuity at $a = 50 \text{ \AA}$ is due to the transition from PAH optical properties to graphite properties above $a_{\xi} = 50 \text{ \AA}$. The upper axis label give the number of carbon atoms $N_C = 0.468(a/\text{\AA})^3$.

$$+ (1 - \phi_{\text{ion}}) \left(\frac{dP}{dE} \right)_{\text{carb}^0} C_{\text{abs}}^{\text{carb}^0}(a, \lambda) B_{\lambda}(T_{\text{carb}^0}[E, a]) \Big] \Big\} \times \left[1 + \frac{u_{\lambda}}{8\pi hc/\lambda^5} \right], \quad (26)$$

where $C_{\text{abs}}^{\text{sil}}$, $C_{\text{abs}}^{\text{gra}}$, $C_{\text{abs}}^{\text{carb}^+}$, and $C_{\text{abs}}^{\text{carb}^0}$ are the absorption cross sections for silicate grains, graphitic grains, and neutral and ionized carbonaceous grains, respectively; \bar{T}_{sil} , \bar{T}_{gra} are the equilibrium temperatures of silicate and graphite grains, respectively; $dP(E)$ is the probability that the grain vibrational energy will be in $[E, E + dE]$; and $T_x(E, a)$ is the effective vibrational temperature for a grain with composition x , vibrational energy E , and radius a (see DL01). The first term on the right represents the contribution of big silicate grains ($a \geq 250\text{\AA}$; hereafter “B_{sil}”); the second term represents the big carbonaceous grain component ($a \geq 250\text{\AA}$; hereafter “B_{carb}”); the third term represents the very small silicate component ($3.5\text{\AA} \leq a < 250\text{\AA}$; hereafter “S_{sil}”); the fourth and fifth terms represent the charged and neutral very small carbonaceous grains (including PAHs) for $3.5\text{\AA} \leq a < 250\text{\AA}$; hereafter “S_{carb}”. The $u_{\lambda}/(8\pi hc/\lambda^5)$ factor is a (usually negligible) correction for stimulated emission. In regions where dust is optically thin to its own thermal emission, the resulting IR intensity is simply

$$(I_{\lambda})_{\text{dust}} = E_{\lambda}(\chi) \times N_{\text{H}} \quad (27)$$

where N_{H} is hydrogen column density. Dust self-absorption should be taken into account in regions with large N_{H} :

$$(I_{\lambda})_{\text{dust}} = E_{\lambda}(\chi) \times \frac{1 - \exp[-N_{\text{H}}\Sigma_{\text{abs}}(\lambda)]}{\Sigma_{\text{abs}}(\lambda)} \quad (28)$$

where $\Sigma_{\text{abs}}(\lambda)$ is the total absorption⁶ cross section per H nucleon for the dust model.

10. Model Emission Spectra and Observations

10.1. Overview of Model Parameters

If we choose a value for σ (we take $\sigma = 0.4$), then the grain model has a total of 18 adjustable parameters:

1. q_{gra} , determining the PAH near-IR continuum ($1\text{--}5\mu\text{m}$) opacity; we take $q_{\text{gra}} = 0.01$ (see §2.2, §2.4);
2. a_{ξ} , determining the transition from PAH optical properties to graphite properties; we take $a_{\xi} = 50\text{\AA}$ (see §2.2);
3. $a_{\text{t,sil}}$, $a_{\text{c,sil}}$, α_{sil} , β_{sil} , C_{sil} , $a_{\text{t,carb}}$, $a_{\text{c,carb}}$, α_{carb} , β_{carb} , C_{carb} , characterizing the size distributions and abundances of silicate and carbonaceous grains (§7);
4. a_{01} , $b_{\text{C},1}$, a_{02} , $b_{\text{C},2}$ ($= b_{\text{C}} - b_{\text{C},1}$), characterizing the size distributions and abundances of the two log-normal components of very small carbonaceous grains (§7);
5. χ_{MMP} , the starlight intensity (§4);
6. N_{H} , the total column density of material.

In addition, the spectrum depends on the ionized fraction $\phi_{\text{ion}}(a)$ for PAHs, determined by χ_{MMP}/n_e (n_e is the electron number density) and the gas temperature T .

⁶If the radiation field in the emitting region is approximately isotropic, scattering does not alter the intensity.

For the UV properties of PAHs adopted here, WD01 show that the observed interstellar extinction puts an upper limit on $b_C = b_{C,1} + b_{C,2} \lesssim 60$ ppm for the average extinction in diffuse regions (WD01). For a given choice of $b_C \leq 60$ ppm, ten of the parameters ($a_{t,\text{sil}}$, $a_{c,\text{sil}}$, α_{sil} , β_{sil} , C_{sil} , $a_{t,\text{carb}}$, $a_{c,\text{carb}}$, α_{carb} , β_{carb} , C_{carb}) are determined by fitting the interstellar extinction curve (see WD01a).

The strength of the 5–12 μm IRTS spectrum relative to the total far infrared emission in the MIRS region requires a population of PAHs with $b_{C,1} \approx 45$ ppm with a mass distribution peaking near ~ 6 Å. Thus $a_{01} \approx 6 \text{ Å} \exp(-3\sigma^2)$; adopting $\sigma = 0.4$ gives $a_{01} \approx 3.5 \text{ Å}$.

For the high galactic latitude dust we take $\chi_{\text{MMP}} = 1$, since the starlight heating this nearby, optically-thin diffuse material should be very close to the local ISRF estimate of Mathis, Mezger, & Panagia (1983).

The dust at high galactic latitudes has substantially more 60 μm emission than would be produced by graphite and silicate grains at their “thermal equilibrium” temperatures \bar{T} . Within the context of the graphite-silicate model, we can account for this extra emission with a population of very small carbonaceous grains which undergo single-photon heating to $T \approx 40$ K, which corresponds to $a \approx 50$ Å grains. We therefore add $b_{C,2} \approx 15$ ppm in a population of grains with $a_{02} \approx 50 \text{ Å} \exp(-3\sigma^2) \approx 30 \text{ Å}$.

This completes specification of the properties of our “standard” grain model, with parameters summarized in Table 3. To compute the emission, it remains only to specify the intensity of the starlight heating the grains, and the total column density N_{H} .

10.2. Observational Constraints

We will compare our model results with observational data for 3 regions: the average emission per H observed by DIRBE (Arendt et al. 1998) and FIRAS (Finkbeiner et al. 1999) for high-Galactic-latitude regions; the DIRBE flux and the 4.5–11.7 μm IRTS spectrum (Onaka et al. 1996) for the “MIRS” region; and the DIRBE flux and the 2.8–3.9 μm IRTS spectrum (Tanaka et al. 1996) for the “NIRS” region. For the MIRS and NIRS regions the DIRBE fluxes were obtained from the DIRBE data set, obtained from the National Space Science Data Center (NSSDC). In Table 4 we list the DIRBE fluxes for these three regions.

Table 3: Parameters for standard dust model for $R_V = 3.1$

PAHs	carbonaceous ^a	silicate ^a
$b_{C,1}=45\text{ppm}$, $a_{01}=3.5\text{Å}$ ($\sigma=0.4$)	$a_{t,\text{carb}} = 0.0107\mu\text{m}$	$a_{t,\text{sil}} = 0.164\mu\text{m}$
$b_{C,2}=15\text{ppm}$, $a_{02}=30\text{Å}$ ($\sigma=0.4$)	$a_{c,\text{carb}} = 0.428\mu\text{m}$	$a_{c,\text{sil}} = 0.100\mu\text{m}$
$a_\xi=50\text{Å}$, $q_{\text{gra}} = 0.01$	$\alpha_{\text{carb}} = -1.54$	$\alpha_{\text{sil}} = -2.21$
$E_{6.2} = 3$, $E_{7.7} = E_{8.6} = 2^b$	$\beta_{\text{carb}} = -0.165$	$\beta_{\text{sil}} = 0.30$
H/C from eq. (4)	$C_{\text{carb}} = 9.99 \times 10^{-12}$	$C_{\text{sil}} = 1.00 \times 10^{-13}$

^aTaken from Weingartner & Draine (2001a).

^bSee Table 1.

10.3. Model Spectra: High-Galactic-Latitude Emission

The high galactic latitude regions are optically thin to starlight, so the starlight illuminating the grains is approximately uniform, with intensity $\chi_{\text{MMP}} \approx 1$. We adopt our standard grain model, with parameters from Table 3.

Arendt et al. (1998) have determined $\Delta I_\lambda / \Delta N_{\text{H}}$, which we compare with $E_\lambda(\chi)$ from eq. (27). In Figure 8 we show $\lambda I_\lambda / N_{\text{H}}$ for our dust model for $\chi_{\text{MMP}} = 1$. The model is in excellent agreement with the observed dust emission per H nucleon for $\lambda \geq 100\mu\text{m}$. At $60\mu\text{m}$ the model emission is $\sim 18\%$ low, which is probably within the uncertainties in the DIRBE fluxes⁷ and the uncertainties in subtraction of zodiacal emission in high galactic latitude regions (Arendt et al. 1998). There is a significant discrepancy between model and observation at $12\mu\text{m}$, where the model flux is only 55% of the observed flux. In view of the difficulties in correction for zodiacal emission, which is relatively strong at $12\mu\text{m}$, the shortfall at $12\mu\text{m}$ may not be real. However, agreement at $12\mu\text{m}$ could be improved if the PAH ionization fraction $\phi_{\text{ion}}(a)$ were reduced for $6 \lesssim a \lesssim 10 \text{ \AA}$, since in this size range the strong $7.7\mu\text{m}$ feature in ionized PAHs radiates away energy at the expense of the 11.3, 11.9, and $12.7\mu\text{m}$ C-H out-of-plane bending modes. Unfortunately, there are as yet no observational data regarding the strength of the 6.2, 7.7, and $8.6\mu\text{m}$ emission from high galactic latitudes.

The model emission also appears to fall short at $5\mu\text{m}$, where the model flux is only 40% of the observed value. At these shorter wavelengths correction for zodiacal emission is increasingly difficult. However, if the reported $\Delta I_\lambda / \Delta N_{\text{H}}$ is correct it would require additional opacity at this wavelength for the ultrasmall grain component. Such additional opacity could, for example, be contributed by carbon chain molecules with a carbon abundance of $\lesssim 1\text{ppm}$ (Allamandola et al. 1999b).

The far-IR–submillimeter emission from dust at high galactic latitudes has been measured by FIRAS (Wright et al. 1991; Reach et al. 1995; Finkbeiner et al. 1999). In Figure 9 we show the average FIRAS spectrum from Finkbeiner et al. (1999) together with the far-IR emission calculated for our grain model, for grains illuminated by $\chi_{\text{MMP}} = 1$. Even using the original DL84 dielectric functions for graphite and silicate, the model is in very good quantitative agreement with the FIRAS measurements for $\lambda < 1100\mu\text{m}$. The agreement is improved if the silicate emissivity is modified for $\lambda > 250\mu\text{m}$, as described in §2.1. The resulting emission spectrum is then in excellent agreement with the observations. Finkbeiner et al. (1999) had argued that the FIRAS spectrum was indicative of two types of dust grains, one of which was quite

⁷Dwek et al. [1997] have estimated that the DIRBE fluxes have $1\text{-}\sigma$ uncertainties of $\pm 20\%$.

Table 4: DIRBE results for high galactic latitudes and NIRS and MIRS regions .

Item	$2.2\mu\text{m}$	$3.5\mu\text{m}$	$4.9\mu\text{m}$	$12\mu\text{m}$	$25\mu\text{m}$	$60\mu\text{m}$	$100\mu\text{m}$	$140\mu\text{m}$	$240\mu\text{m}$
$\lambda_{\text{effective}} (\mu\text{m})$	2.22	3.53	4.88	12.3	20.8	56.0	97.7	148	248
FWHM (μm)	0.37	0.97	0.67	8.1	8.9	27.3	31.0	35	101
HGL ^a	-	0.97	1.11	7.16	3.57	5.30	18.6	22.5	10.1
MIRS region ^b	6.65	3.47	1.68	3.79	2.10	4.85	11.5	19.4	8.20
NIRS region ^c	7.13	3.47	1.55	3.01	1.58	3.63	9.01	14.9	6.27

^a $\Delta(\lambda I_\lambda) / \Delta N_{\text{H}}$ for $|b| \gtrsim 25^\circ$ ($10^{-26} \text{ erg s}^{-1} \text{ sr}^{-1} \text{ H}^{-1}$) (Arendt et al. 1998).

^b λI_λ ($10^{-3} \text{ erg s}^{-1} \text{ cm}^{-2} \text{ sr}^{-1}$) for $44^\circ \leq l \leq 44^\circ 40'$, $-0^\circ 40' \leq b \leq 0^\circ$ (Hauser et al. 1998).

^c λI_λ ($10^{-3} \text{ erg s}^{-1} \text{ cm}^{-2} \text{ sr}^{-1}$) for $47^\circ 30' \leq l \leq 48^\circ$, $|b| \leq 15'$ (Hauser et al. 1998).

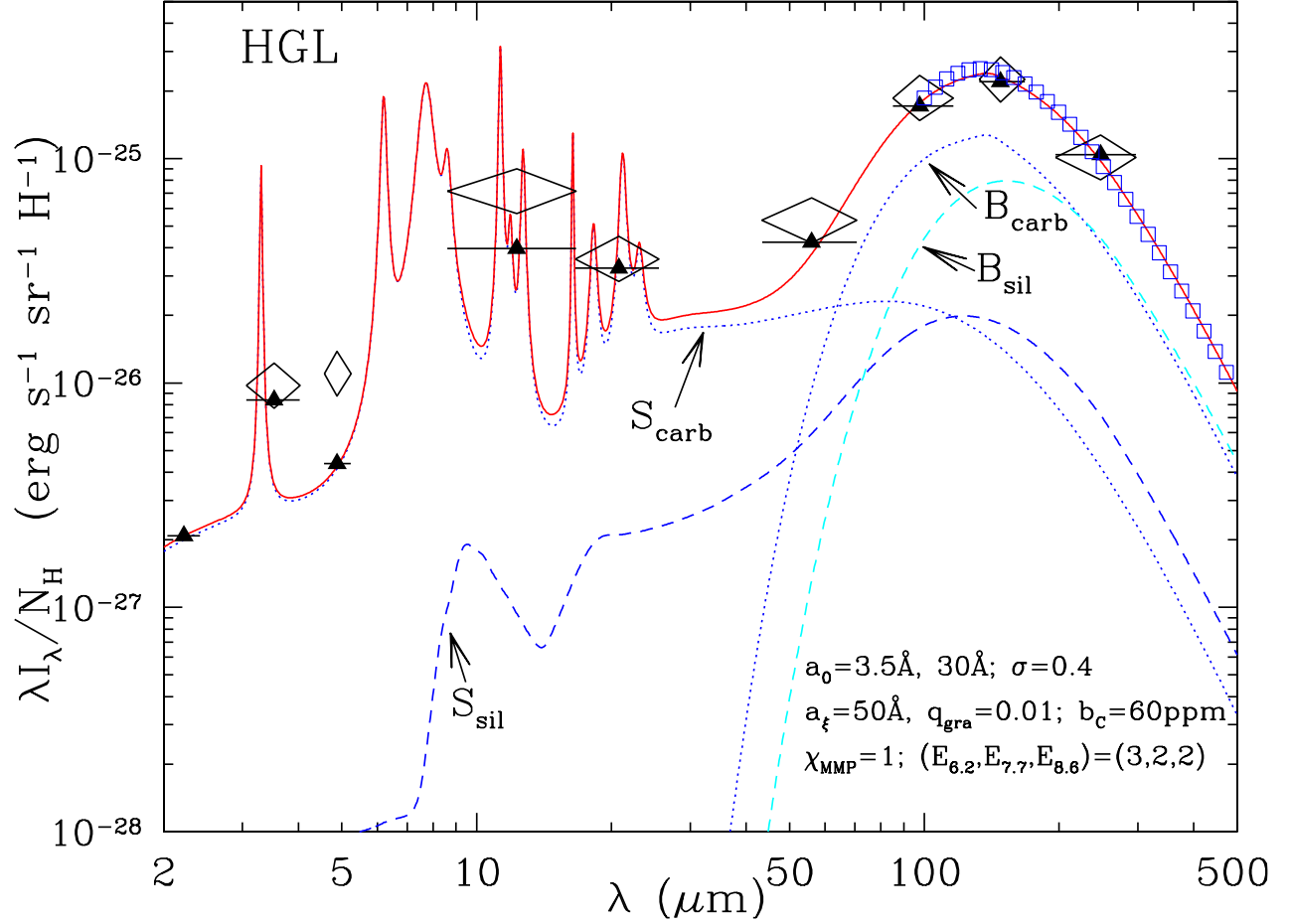


Fig. 8.— Comparison of the model to the observed emission from the diffuse ISM at high galactic latitudes ($|b| \geq 25^\circ$). Curves labelled B_{sil} and B_{carb} show emission from “big” ($a \geq 250 \text{ \AA}$) silicate and carbonaceous grains; curves labelled S_{sil} and S_{carb} show emission from “small” ($a < 250 \text{ \AA}$) silicate and carbonaceous grains (including PAHs). Triangles show the model spectrum (solid curve) convolved with the DIRBE filters. Observational data are from DIRBE (diamonds; Arendt et al. 1998), and FIRAS (squares; Finkbeiner et al. 1999).

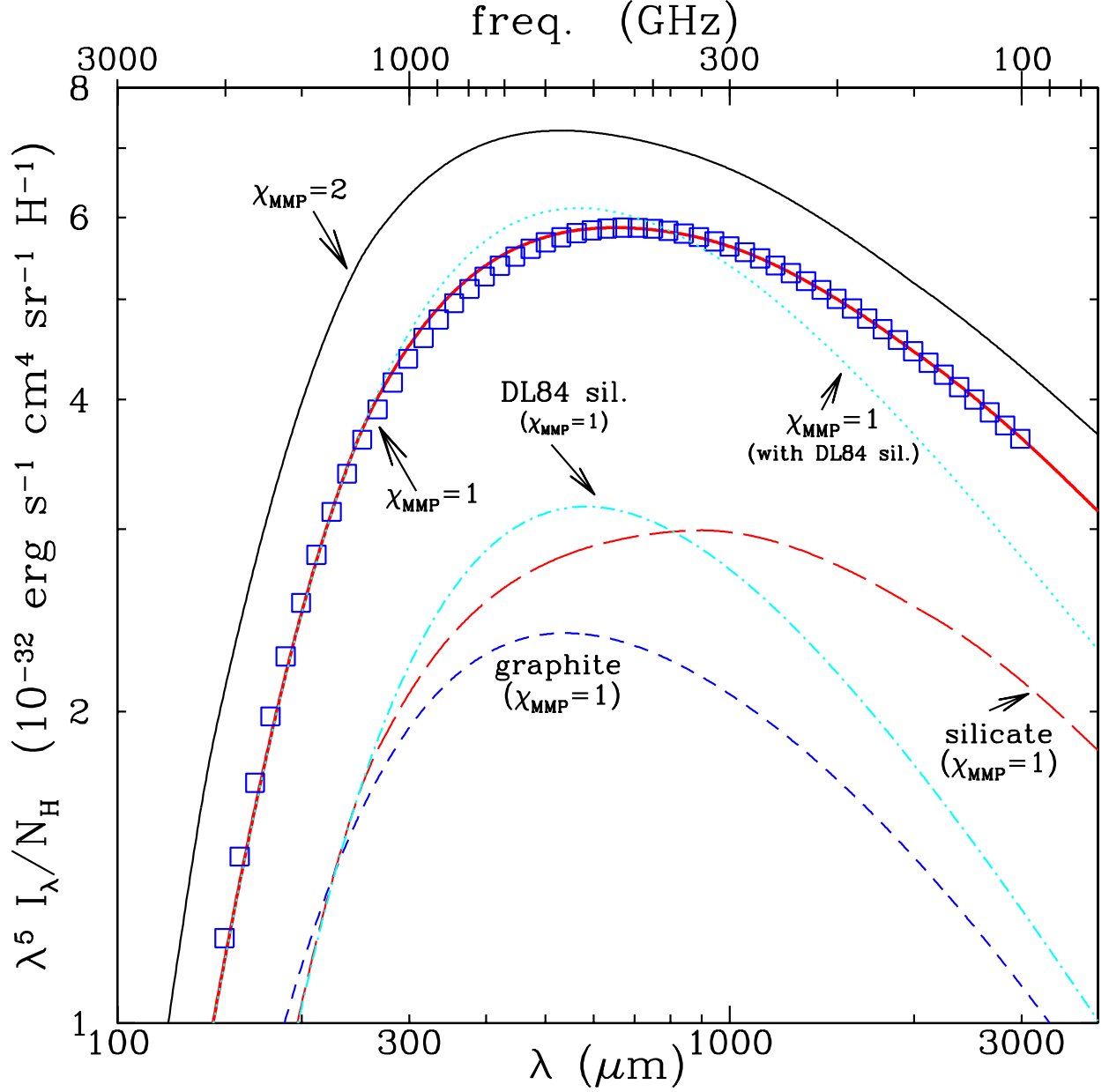


Fig. 9.— The far-IR spectrum per H nucleon. Squares are the FIRAS data represented by a “two-temperature” fit (Finkbeiner et al. 1999). Dotted line shows model spectra for $\chi_{\text{MMP}} = 1$, calculated using the silicate dielectric function from DL84. Solid lines are model spectra for $\chi_{\text{MMP}} = 1$ and 2, labelled by the value of χ_{MMP} , calculated using the modified silicate dielectric function from the present work (see §2.1). The model for $\chi_{\text{MMP}} = 1$ closely reproduces the observed FIRAS emission (as discussed in §2.1, the silicate dielectric function at $\lambda > 250\mu\text{m}$ has been modified slightly to improve the agreement). Broken lines show the contribution of carbonaceous grains and silicate grains to the emission for $\chi_{\text{MMP}} = 1$ (dot-dashed line shows emission calculated using DL84 silicate dielectric function).

cold. However, we see here that the “graphite-silicate” grain model, with the silicate emission modified by no more than $\pm 12\%$ for $\lambda < 1100\mu\text{m}$, gives essentially perfect agreement with the FIRAS spectra.

10.4. Model Spectra: Galactic Plane Regions

The DIRBE short wavelength channels are dominated by starlight. We model the DIRBE spectra by taking

$$I_\lambda = (I_\lambda)_{\text{dust}} + A \left[\sum_{i=2}^4 W_i B_\lambda(T_i) \right] \frac{1 - \exp[-N_H \Sigma_{\text{abs}}(\lambda)]}{\Sigma_{\text{abs}}(\lambda)}, \quad (29)$$

where $(I_\lambda)_{\text{dust}}$ is obtained from eq. (28), the multiplicative factor A determines the strength of the starlight, and the W_i and T_i are the same as for the ISRF (see §4). Equation (29) would be exact if the stellar density was proportional to the dust density and the starlight was isotropic at all points along the line of sight (so that scattering does not alter the intensity). While not expected to be highly accurate, this approximation should give a reasonable approximation to the overall spectrum.

We adopt our “standard” grain model (see Table 3). This assumes that the dust in the 6 kpc molecular ring (where most of the interstellar matter in the MIRS and NIRS fields is located) has the same size distribution as dust in the local diffuse ISM; this assumption is likely to be incorrect in detail, but is the best we can do at this time.

10.4.1. Single- χ Models

The grains in the MIRS and NIRS Galactic plane regions will be illuminated by a range of radiation fields, since each $0.5^\circ \times 0.5^\circ$ field (52 pc \times 52 pc @ 6 kpc) will include diffuse clouds, molecular clouds and star-forming regions. The simplest approximation is to assume that the dust is uniformly distributed in the beam and heated by a uniform radiation field with intensity χ_{MMP} relative to the local ISRF. For a given χ_{MMP} , the column density N_H is adjusted to match the DIRBE $140\mu\text{m}$ intensity. The constant A in eq. (29) determining the strength of the stellar contribution has been adjusted so that the spectrum agrees with the DIRBE $3.5\mu\text{m}$ measurement. We find that the $\chi_{\text{MMP}}=2$ model provides a rough overall fit to the IRTS spectra and DIRBE photometry.

In Figure 10 we show the emission spectrum calculated for the “standard” dust model, for grains heated by $\chi_{\text{MMP}} = 2$, for both the MIRS and NIRS regions. Note that the model spectra have been smoothed to the resolution of the NIRS and MIRS instruments on IRTS for comparison with the IRTS spectra. Also note that the column densities N_H are very large, corresponding to $A_V = 23$ and 17 mag for the MIRS and NIRS regions, respectively. These column densities are large enough so that self-absorption is significant at $\lambda \lesssim 15\mu\text{m}$. In particular, the 3.3, 6.2, and 11–12 μm features are noticeably attenuated by the dust absorption.

This simple model provides fair agreement with the DIRBE observations of these two fields. The largest discrepancy is at $100\mu\text{m}$, where the observed flux is only 70% of the model value.

The model is in reasonably good agreement with the IRTS 5–12 μm spectrum in the MIRS region. The model is $\sim 40\%$ below the 11.3 μm peak observed by IRTS, and $\sim 32\%$ below the DIRBE 12 μm measurement, but note that 1) the claimed absolute calibration accuracy of the MIRS instrument is only $\pm 30\%$ (Onaka et

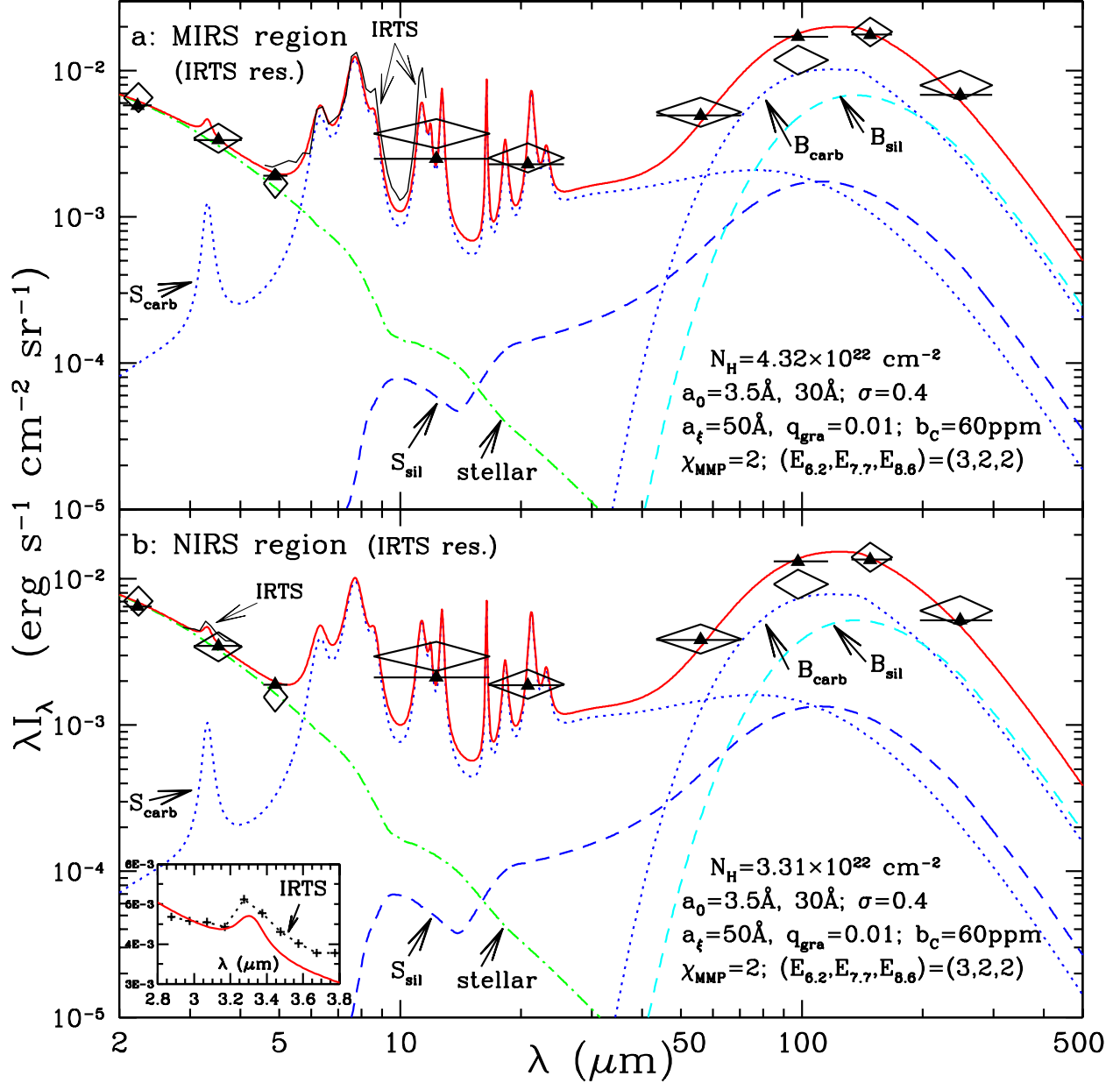


Fig. 10.— Infrared emission from dust plus starlight (see text) for two regions in the Galactic plane: (a) the MIRS region ($44^\circ \leq l \leq 44^\circ 40'$, $-0^\circ 40' \leq b \leq 0^\circ$), and (b) the NIRS region ($47^\circ 30' \leq l \leq 48^\circ$, $|b| \leq 15'$). For both regions we use our standard dust parameters, with the PAH ionization fraction ϕ_{ion} (a) taken to be the weighted mean for the local ISM (43% CNM, 43% WNM, 14% WIM). The starlight intensity heating the dust has been taken to be $\chi_{\text{MMP}} = 2$. The solid curve shows the overall model spectrum, degraded to the IRTS resolution; triangles show the model spectrum convolved with the DIRBE filters. DIRBE observations are shown as diamonds. For the MIRS field we show the IRTS MIRS 5–12 μm spectrum (thin solid line). For the NIRS field we show the IRTS NIRS 2.8–3.9 μm spectrum (thin solid line, also shown as cross-dotted curve in inset). Curves labelled B_{sil} and B_{carb} show emission from “big” ($a \geq 250 \text{ \AA}$) silicate and carbonaceous grains; curves labelled S_{sil} and S_{carb} show emission from “small” ($a < 250 \text{ \AA}$) silicate and carbonaceous grains (including PAHs).

al. 1996), 2) the DIRBE photometric accuracy is estimated to be $\pm 20\%$ (Dwek et al. 1997).

The model is also in reasonably good agreement with the IRTS NIRS 2.8–3.9 μm spectrum in the NIRS region. Recall that the stellar contribution has been adjusted to match the DIRBE 3.5 μm photometry; with this choice of stellar continuum, the model falls $\lesssim 15\%$ below the NIRS spectrophotometry for $\lambda < 3.7\mu\text{m}$. This agreement is satisfactory, since the difference of the overall slope of the 2.8–3.9 μm NIRS spectrum and the slope indicated by the DIRBE 2.2, 3.5, and 4.9 μm photometry suggests that the uncertainties in the NIRS spectrophotometry may exceed the claimed $\pm 5\%$ absolute calibration uncertainty (Tanaka et al. 1996). The model prediction for the strength of the 3.3 μm emission feature is in good agreement with the NIRS photometry (see the inset in Figure 10b).

In the context of the single- χ model, dust models with either weaker or stronger radiation fields are less successful than the $\chi_{\text{MMP}}=2$ model in reproducing the observed spectra. The $\chi_{\text{MMP}}=1$ model does not emit sufficiently at 5–12 μm due to self-absorption by the very large column density of dust; on the other hand, the $\chi_{\text{MMP}}=3$ model, although providing a reasonably good fit to the 5–12 μm spectrum, emits too much (by $\gtrsim 75\%$) at 100 μm .

10.4.2. Multi- χ Models

The overprediction of the 100 μm flux in Figure 10 could be due in large part to the simplification of assuming that all of the dust is heated by a single radiation field. Consider instead a model where a fraction f_j of the dust is heated by starlight with intensity χ_j . If the regions of different χ_j are randomly located on scales small compared to the beamsize, then we may approximate the different dust emissivities as uniformly mixed, so that the emergent intensity becomes

$$(I_\lambda)_{\text{dust}} = \left[\sum_j f_j E_\lambda(\chi_j) \right] \frac{1 - \exp[-N_{\text{H}} \Sigma_{\text{abs}}(\lambda)]}{\Sigma_{\text{abs}}(\lambda)}. \quad (30)$$

The $\chi_{\text{MMP}} = 2$ model of Figure 10 exceeds the observed 100 μm emission by about 40%. This might indicate that the dust used to reproduce the 140 μm emission is somewhat too hot. We can try to remedy this by using cold dust to provide the 140 and 240 μm emission, plus additional warmer dust to provide sufficient 60 μm emission. Two examples of multi- χ models for the MIRS region are shown here. In Figure 11a we show a multi- χ model where the cooler dust is heated by $\chi_{\text{MMP}} = 0.7$, and the warmer dust by $\chi_{\text{MMP}} = 100$. This model reproduces the 60, 100, 140, and 240 μm photometry, but the mid-IR absorption by the large amount of cool dust causes the 11–12 μm emission to be too low by more than a factor of two. If the cooler dust is taken to be heated by $\chi_{\text{MMP}} = 1$, we obtain Figure 11b. This model now exceeds the observed 100 μm flux by $\sim 20\%$. The total dust column density has been reduced by $\sim 30\%$ compared to Figure 11a, but is still $\sim 80\%$ greater than in the single- χ model of Figure 10a – there is sufficient absorption at 12 μm that this model falls short of the observed flux by $\sim 30\%$. We have also carried out calculations for models combining three or more χ values and found no significant improvement. We conclude that multi- χ models offer no significant improvement over the simple single- χ model of §10.4.1.

10.5. Emission Spectra for Different Starlight Intensities

In §10.3 we have shown models for optically-thin emission from our standard model heated by starlight with $\chi_{\text{MMP}} = 1$ for the high-latitude dust. To study the sensitivity to the assumed starlight intensity, in

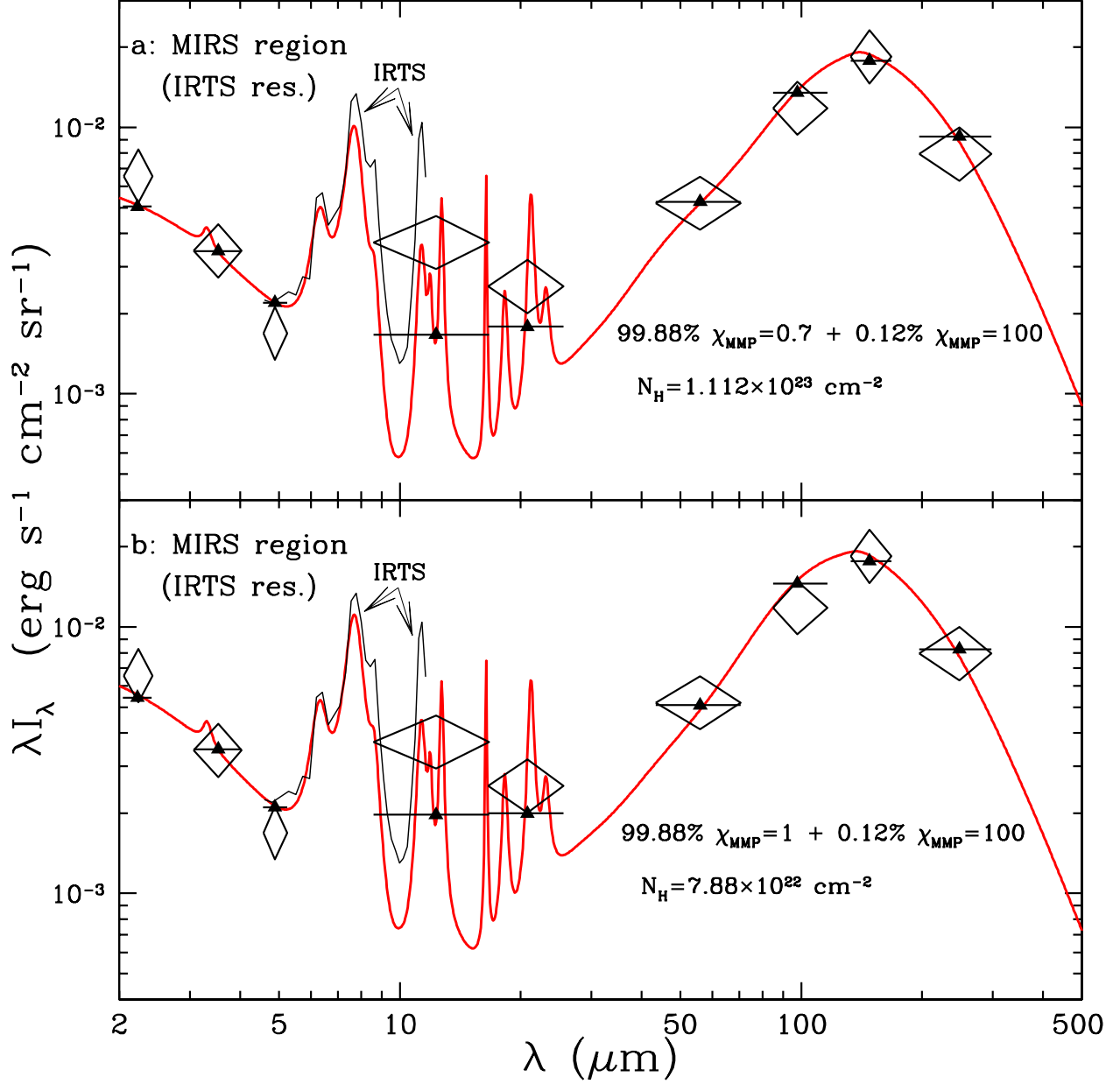


Fig. 11.— Same as Figure 10a, but for multi- χ models. Upper panel: a model where the far-IR emission is provided by dust with $\chi_{\text{MMP}} = 0.7$, with additional emission from dust heated by $\chi_{\text{MMP}} = 100$. While providing good agreement with the 60–240 μm DIRBE fluxes, the model is a factor of two low in the 12 μm region, partly due to the absorption contributed by the very large column density of $\chi_{\text{MMP}} = 0.7$ dust. Lower panel: a model where the far-IR emission is provided by dust heated by $\chi_{\text{MMP}} = 1$, with additional emission from dust with $\chi_{\text{MMP}} = 100$. There is less dust absorption, but the model still falls short in the 12 μm region.

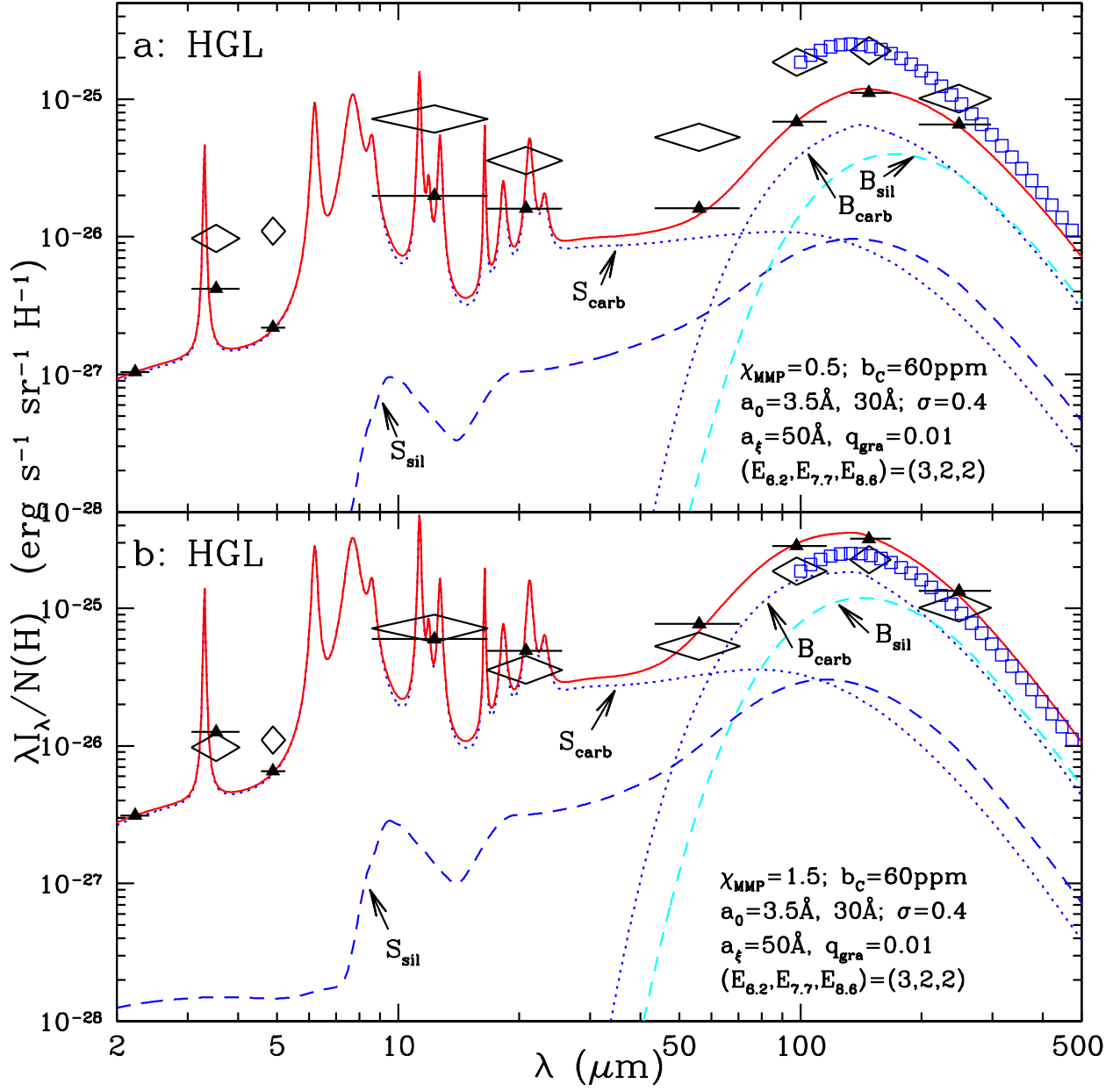


Fig. 12.— As in Figure 8, but for dust illuminated by starlight intensities $\chi_{\text{MMP}} = 0.5$ (upper panel) or $\chi_{\text{MMP}} = 1.5$ (lower panel).

Figure 12 we show spectra for $\chi_{\text{MMP}} = 0.5$ and 1.5. As expected from Figure 8, the $\chi_{\text{MMP}} = 0.5$ model yields too little emission (by $\approx 50\%$) over the entire spectral range; the $\chi_{\text{MMP}}=1.5$ model emits too much at $\lambda \gtrsim 50\mu\text{m}$.

Finally, in Figure 13 we show the emission from dust heated by radiation fields with $\chi_{\text{MMP}} = 0.3, 1, 3, 10, 100, 10^3, 10^4$ (we assume all have the same ϕ_{ion} as the local ISM). We see that the fraction of the infrared emission emerging at $\lambda < 30\mu\text{m}$ is relatively independent of χ_{MMP} (over this range), since this part of the spectrum is dominated by single-photon heating. This naturally explains why the observed PAH emission features show little spectral change in various regions with UV intensities differing by five orders of magnitude (e.g., see Boulanger 1999). However, as expected, the emission at $\lambda \gtrsim 50\mu\text{m}$ shows a shift from longer to shorter wavelengths as χ_{MMP} is increased from 0.3 to 10^4 .

The *Space Infrared Telescope Facility* (SIRTF) will be capable of sensitive imaging using the *Infrared Array Camera* (IRAC) at 3.6, 4.5, 5.8, and $8.0\mu\text{m}$, and using the *Multiband Imaging Photometer* (MIPS) at 24, 70, and $160\mu\text{m}$. In Table 5 we show the band-averaged intensities for our standard dust model heated by starlight radiation fields of various intensities.

Table 5: I_ν/N_{H} ($\text{MJy sr}^{-1}/10^{20} \text{ cm}^{-2}$) Averaged over SIRTf Bands for Standard Dust Model Illuminated by Starlight Intensity χ_{MMP} .

χ_{MMP}	IRAC 3.6 μm	IRAC 4.5 μm	IRAC 5.8 μm	IRAC 8.0 μm	MIPS 24 μm	MIPS 70 μm	MIPS 160 μm
0.3	3.49×10^{-4}	1.63×10^{-4}	2.02×10^{-3}	7.30×10^{-3}	8.88×10^{-3}	0.0311	0.373
1	1.16×10^{-3}	5.45×10^{-4}	6.75×10^{-3}	0.0243	0.0302	0.188	1.200
3	3.49×10^{-3}	1.63×10^{-3}	0.0202	0.0726	0.0937	0.932	2.96
10	0.0116	5.45×10^{-3}	0.0675	0.243	0.335	4.51	6.85
100	0.116	0.0545	0.677	2.44	4.35	52.4	24.2
10^3	1.17	0.548	6.82	25.1	81.5	331	64.3
10^4	11.8	5.61	71.7	290	1690	1330	143

10.6. PAH Feature Strengths and the H/C Ratio

Our standard model assumes enhancements $E_{6.2,7.7,8.6} = (3, 2, 2)$ of the PAH band strengths. To demonstrate the need for such enhancement, in Figure 14a we plot the best-fitting model using the *laboratory-measured* PAH feature strengths [i.e. $E_{6.2,7.7,8.6} = (1, 1, 1)$]. Although the fit to the $11.3\mu\text{m}$ peak becomes a little better than our “standard” model (Figure 10a), the fit to the 6.2, 7.7, $8.6\mu\text{m}$ region is not as good as the standard model. We also note that the fit does not necessarily get improved by increasing the PAH feature strengths by a *larger* factor as expected from energy conservation consideration.

Previous sections all assume a H/C ratio representing compact, symmetric PAHs (eq. [4], §2.3). For PAHs with open, uneven structures (e.g., elongated PAHs), the H/C ratio is expected to be higher. With this in mind, we consider a dust model with a relatively higher H/C ratio

$$\text{H/C} = \begin{cases} 0.5, & N_{\text{C}} \leq 60, \\ 0.5/\sqrt{N_{\text{C}}/60}, & 60 \leq N_{\text{C}} \leq 240, \\ 0.25, & N_{\text{C}} \geq 240. \end{cases} \quad (31)$$

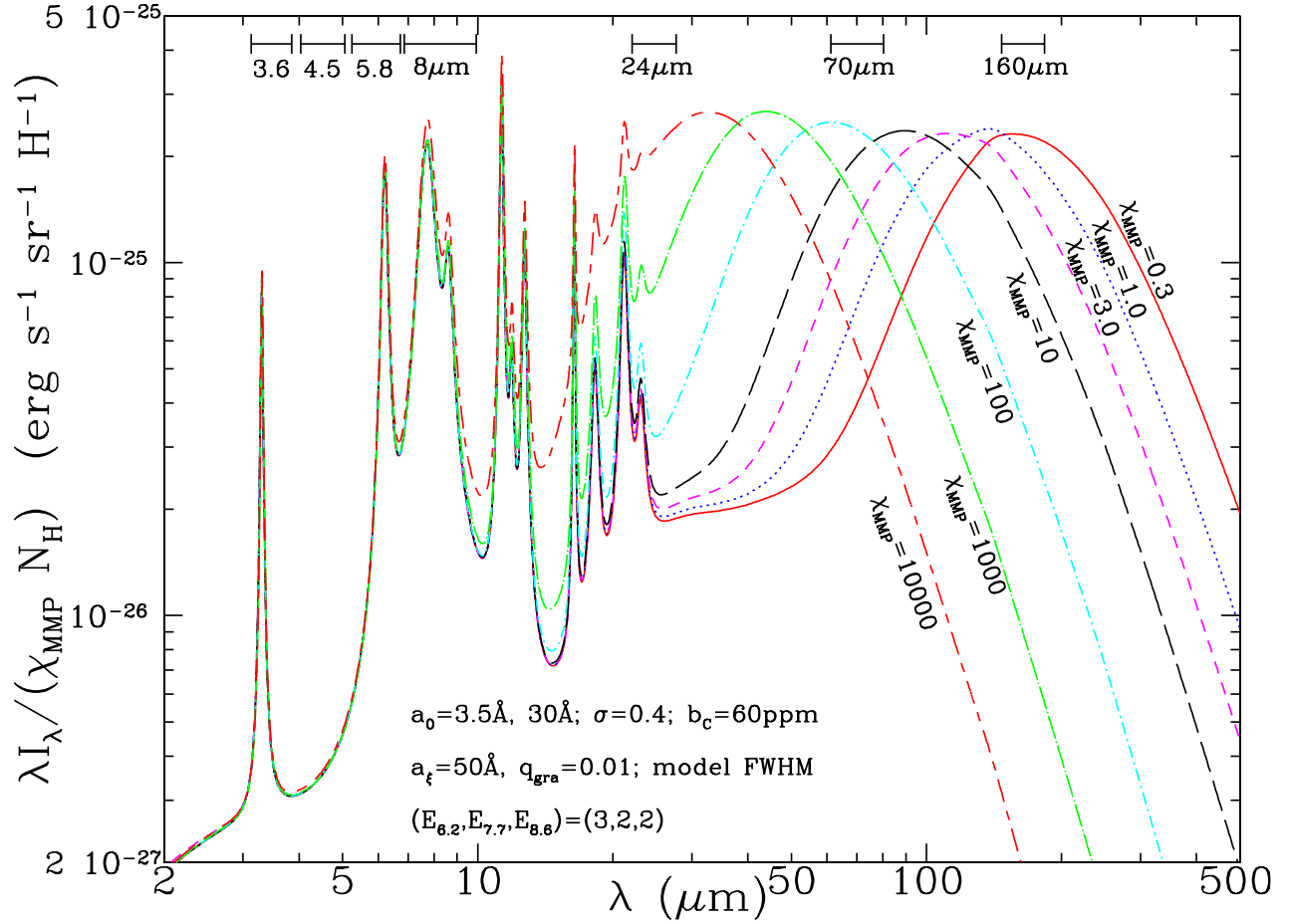


Fig. 13.— IR spectra (scaled by the starlight intensity) for our standard grain model for different illuminating radiation fields. The overall shape for $\lambda \lesssim 15 \mu\text{m}$ is almost unchanged for regions with starlight intensities varying by about five orders of magnitude. Note we have assumed the same ionization fraction (ϕ_{ion}) as in the local diffuse ISM. We also show the wavelength coverage of the 4 IRAC bands and 3 MIPS bands on SIRTf.

The corresponding spectrum is shown in Figure 14b. The C-H features ($3.3, 8.6, 11.3\mu\text{m}$) become slightly stronger, and the C-C features ($6.2, 7.7\mu\text{m}$) become slightly weaker (as expected from energy conservation), but the entire spectrum is nearly indistinguishable from the model with a lower H/C ratio (eq. [4]; Figure 10a).

The dust model described in this work assumes essentially full hydrogen coverage for PAHs. Dehydrogenation becomes significant only for the smallest PAHs. Upon absorption of an energetic photon, large PAHs will not have CH bond rupture since the absorbed energy will promptly be redistributed among many vibrational modes. Tielens et al. (1987) concluded that small PAHs ($N_C \lesssim 25$) would be partially dehydrogenated in regions with intense UV fields, while large PAHs ($N_C \gtrsim 25$) would be completely hydrogenated in those regions. Allain, Leach & Sedlmayr (1996) reexamined this and reached similar conclusions – as shown in their Figure 10, PAHs with $N_C \gtrsim 30$ in diffuse clouds are almost 100% hydrogenated. Therefore, it is reasonable to assume full hydrogen coverage. Figure 14b shows that the infrared emission spectrum is insensitive to modest changes in the H/C ratio (except for possible effects on the wavelengths and strengths of the C-H, C-C bands upon dehydrogenation [e.g., see Pauzat, Talbi, & Ellinger 1997]).

In regions very rich in H atoms, a PAH molecule may acquire excess H atoms attached to the peripheral C atoms and become “superhydrogenated”. The addition of extra H atoms to PAHs results in a decrease of the level of “aromaticity” and an increase of the level of “aliphaticity” by weakening the strength of the aromatic C-H stretching band and creating new aliphatic C-H stretching bands (Bernstein, Sandford, & Allamandola 1996). The $3.40, 3.46, 3.51$, and $3.56\mu\text{m}$ subfeatures superposed on the shoulder of the $3.3\mu\text{m}$ feature seen in many objects may be explained by such “superhydrogenation” (Schutte et al. 1993; Bernstein et al. 1996). The very strong $8.6\mu\text{m}$ band seen in the compact HII region IRAS 18434-0242 (Roelfsema et al. 1996) may be due to the extra H atoms bonded to internal C atoms, although the presence of non-compact PAH ions can also enhance the $8.6\mu\text{m}$ band (Roelfsema et al. 1996). Due to the lack of sufficient experimental data and quantum chemical calculations, we have not included possible “superhydrogenation” in our model.

10.7. Total Infrared Emission and Optical-UV Albedos

For $\chi_{\text{MMP}} = 1$ our model for the high galactic latitude emission (Figure 8) yields a total infrared intensity $4\pi \int E_\lambda d\lambda = 4.36 \times 10^{-24} \text{ ergs s}^{-1} \text{ H}^{-1}$ (the fractional contributions of S_{carb} , B_{carb} , and silicate grains [$S_{\text{sil}} + B_{\text{sil}}$], are approximately 33%, 37%, and 30%, respectively). As seen from Figures 8 and 9, our model appears to be in excellent agreement with the overall power radiated by interstellar dust.

By contrast, the model of Dwek et al. (1997) radiates $\sim 37\%$ more power per H nucleon ($6.0 \times 10^{-24} \text{ erg s}^{-1} \text{ H}^{-1}$), and the model of Désert et al. (1990) radiates $\sim 59\%$ more power per H nucleon ($6.92 \times 10^{-24} \text{ erg s}^{-1} \text{ H}^{-1}$). These differences are due to the fact that 1) the model of Dwek et al. (1997) has a UV extinction which is higher than the average Galactic extinction curve (see their Figure 4) and probably has lower optical-UV albedos than ours; 2) the albedos predicted by the Désert et al. (1990) model are significantly lower than those of the current model.

In Figure 15 we show the albedos calculated for the present model (also see Figure 15 in Weingartner & Draine [2001a]) together with the dust albedos estimated from observations of the diffuse Galactic light (Lillie & Witt 1976; Morgan, Nandy, & Thompson 1976; Hurwitz, Bowyer, & Martin 1991; Witt, Friedmann, & Sassene 1997). The current model appears to be in good agreement with the observationally-determined albedos. For comparison, Figure 15 also shows the albedo for the grain model of Désert et al. (1990), which evidently has an absorptivity about 20–50% higher than both the current model and observations at

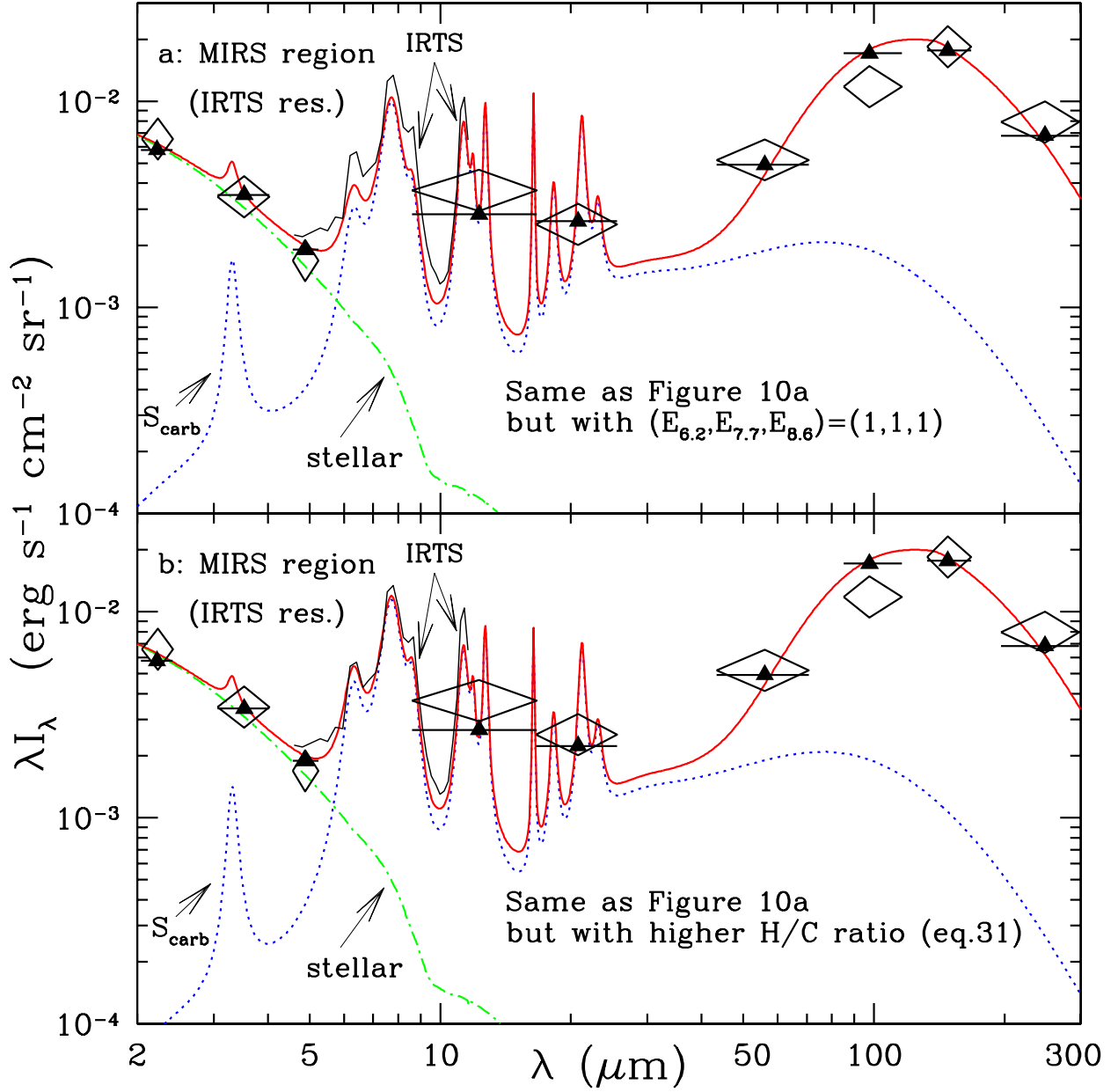


Fig. 14.— (a): Same as Figure 10a but with $(E_{6.2}, E_{7.7}, E_{8.6}) = (1, 1, 1)$. (b): Same as Figure 10a but with a higher H/C ratio (eq. [31]).

$\lambda^{-1} < 4\mu\text{m}^{-1}$ where the bulk of the starlight energy is located.

11. Discussion

Figure 16 compares the extinction curve obtained by our dust model with $b_C = 60\text{ppm}$ ($b_{C,1} = 45\text{ppm}$, $b_{C,2} = 15\text{ppm}$) with the average interstellar extinction curve and also shows the contributions of the individual dust components. It can be seen that PAHs, the dominant contributor to the 2175\AA hump, have a relatively flat behavior for $5 < \lambda^{-1} < 8\mu\text{m}^{-1}$ and thus do not dominate the far-UV extinction. This is consistent with Greenberg & Chlewicki (1983) in which the 2175\AA hump was shown to correlate poorly with the far-UV extinction.

Our dust model implies a total dust mass per H nucleon $m_{\text{dust}} \approx 1.89 \times 10^{-26} \text{ g H}^{-1}$, or a gas-to-dust ratio $1.4m_{\text{H}}/m_{\text{dust}} = 124$. Let $\Sigma_{\text{ext}}(\lambda) \equiv N_{\text{H}}^{-1} \int (dn/da) C_{\text{ext}}(a, \lambda) da$ be the total extinction cross section per H nucleon. The mass absorption coefficient for the dust is just $\kappa_{\text{abs}}(\lambda) = (1 - \text{albedo}) \Sigma_{\text{ext}}(\lambda) / m_{\text{dust}} = 0.4 \ln 10 (1 - \text{albedo}) [A(\lambda) / N_{\text{H}}] / m_{\text{dust}} = 4.88 \times 10^{25} (1 - \text{albedo}) [A(\lambda) / N_{\text{H}}] \text{ cm}^2 \text{ g}^{-1}$. In Table 6 we tabulate κ_{abs} at selected wavelengths. Note that these numbers are for dust in the average diffuse ISM, with $R_V \equiv A_V / E(B - V) \approx 3.1$. In diffuse regions with $R_V > 3.1$ the extinction per H is reduced at $\lambda < 0.9\mu\text{m}$ due to changes in the grain size distribution (see WD01), but the extinction does not appear to be affected at $\lambda \gtrsim 0.9\mu\text{m}$ (Cardelli, Clayton, & Mathis 1989). In dark clouds ice mantle formation adds additional absorption features, most prominently the $3.1\mu\text{m}$ O-H stretch in H_2O , but for $\lambda \gtrsim 10\mu\text{m}$ the opacities in Table 6 probably remain a good approximation even for molecular regions with densities up to $\sim 10^6 \text{ cm}^{-3}$.

Our dust model requires a total of 254ppm of C and 48 ppm of Si in grains, both of which are significantly higher than the maximum available for the dust according to the recent work of Snow & Witt (1995), who suggest that the elemental abundances in the ISM are just 60%–70% of the solar value⁸. However, Weingartner & Draine (2001a) have argued that it is difficult to see how the observed interstellar extinction can be explained if interstellar abundances are appreciably subsolar; they argue that the case for subsolar abundances is not compelling. Dwek (1997) has argued that the composite dust model (Mathis 1996) – which aims at making economical use of dust materials – is still short of carbon when PAHs are included to account for the mid-IR emission.

Our model has an absorption feature at $6.2\mu\text{m}$ due to the PAH C-C stretching mode (see Figure 16). The integrated optical depth of the $6.2\mu\text{m}$ feature relative to the silicate optical depth is $(\int \Delta\tau d\lambda^{-1})_{6.2} / \Delta\tau_{9.7} \approx 2.9 \text{ cm}^{-1}$. The aromatic $6.2\mu\text{m}$ absorption feature has been detected in several objects including both local sources and Galactic center sources (Schutte et al. 1998; Chiar et al. 2000). On average, the observed integrated strength of the $6.2\mu\text{m}$ band per unit silicate band depth is about 2.2 cm^{-1} with no significant difference between the Galactic sources and the local sources (Schutte et al. 1998). Our model is in good agreement with this determination.

In addition to the $6.2\mu\text{m}$ feature, our model also predicts a weak narrow absorption feature at $3.3\mu\text{m}$ with $\int \Delta\tau_{3.3} d\lambda^{-1} / \Delta\tau_{9.7} \approx 0.50 \text{ cm}^{-1}$. This feature has been detected in the Galactic center source GCS 3 with $(\int \Delta\tau d\lambda^{-1})_{3.3} / \Delta\tau_{9.7} \approx 0.34 \text{ cm}^{-1}$ (Chiar et al. 2000). It has also been seen in absorption in some heavily extinguished molecular cloud sight lines (Sellgren et al. 1995; Brooke, Sellgren, & Geballe 1999). The

⁸Although the present model uses more silicon than other existing models, the predicted silicate optical depth $\Delta\tau_{9.7\mu\text{m}} / N_{\text{H}} \approx 3.3 \times 10^{-23} \text{ cm}^2 / \text{H}$ is not inconsistent with observations ($\Delta\tau_{9.7\mu\text{m}} / N_{\text{H}} \approx 2.8 - 5.9 \times 10^{-23} \text{ cm}^2 / \text{H}$; see Draine 1989b, Mathis 1998).

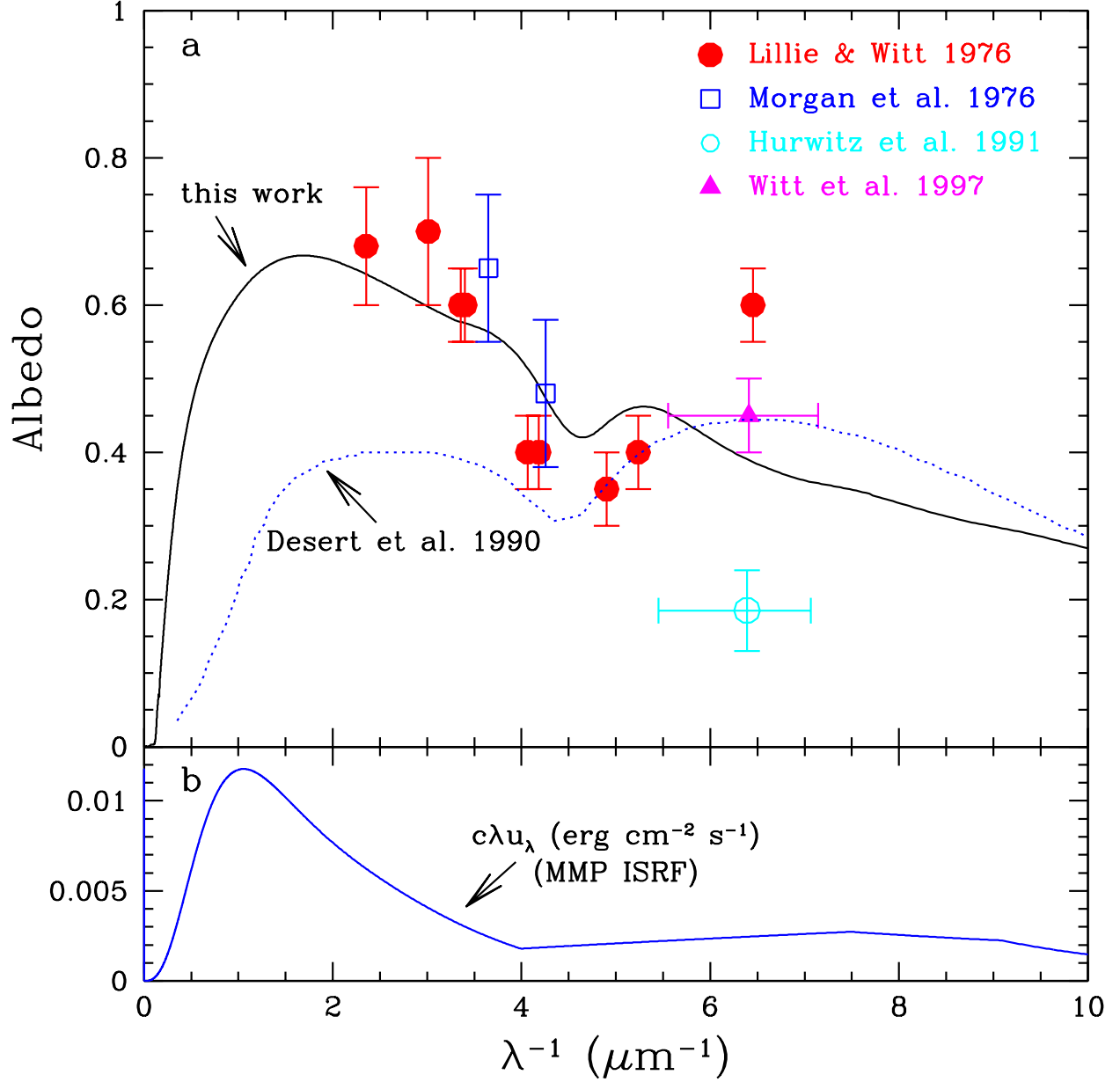


Fig. 15.— (a): Albedo calculated for the present dust model (solid; also see Figure 15 in Weingartner & Draine 2001a) and for the Désert et al. (1990) model (dotted; see their Figure 6) together with observational data for the diffuse Galactic light (filled circles – Lillie & Witt 1976; open squares – Morgan et al. 1976; open circles – Hurwitz et al. 1991; triangles – Witt et al. 1997). (b): The solar neighbourhood ($\chi_{\text{MMP}} = 1$) interstellar radiation field (Mathis et al. 1983). The Désert et al. grain model is much more strongly absorbing at $\lambda^{-1} < 4 \mu\text{m}^{-1}$ where the ISRF energy is concentrated.

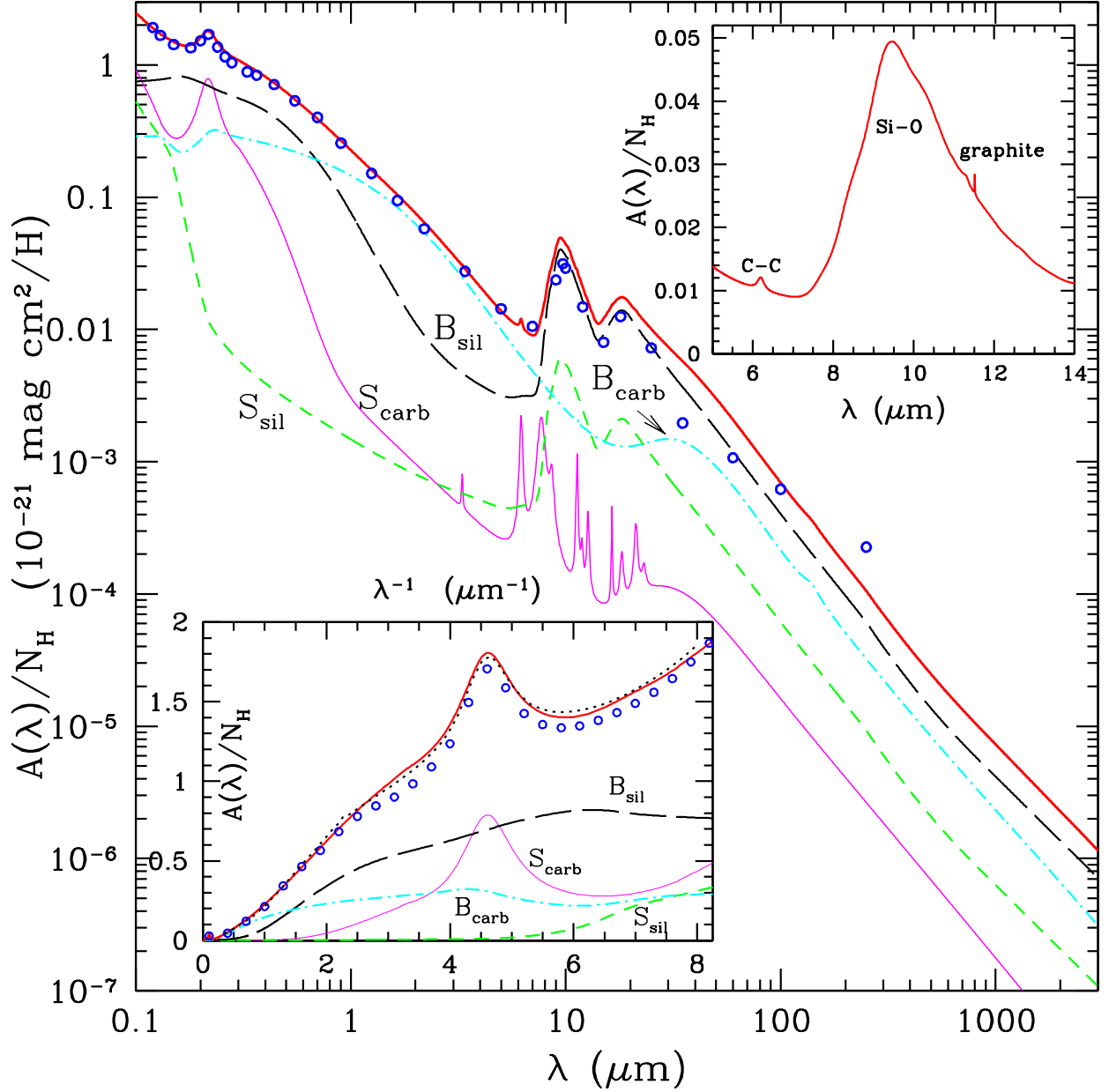


Fig. 16.— The calculated extinction for the present grain model (heavy solid line) and the observed average ($R_V \approx 3.1$) interstellar extinction curve (dotted line: Fitzpatrick 1999; open circles: Mathis 1990). Model results are the sum of 4 components: “ B_{sil} ” (silicate, $a \geq 250\text{\AA}$; long-dashed line); “ S_{sil} ” (silicate, $3.5 \leq a \leq 250\text{\AA}$; short-dashed line); “ B_{carb} ” (carbonaceous, $a \geq 250\text{\AA}$; dot-dashed line); and “ S_{carb} ” (carbonaceous, $3.5 \leq a \leq 250\text{\AA}$, including PAHs; thin solid line). The upper-right inset illustrates the aromatic $6.2\mu\text{m}$ absorption feature and the $9.7\mu\text{m}$ silicate band. The narrow feature at $11.5\mu\text{m}$ is due to a lattice mode of crystalline graphite (Draine 1984) and would likely be smoothed out in an imperfect polycrystalline sample. The lower-left inset plots the extinction curve against λ^{-1} (μm^{-1}).

Table 6. Extinction and absorption properties for dust in the diffuse ISM.^aNOTE: values of Σ_{ext} and κ_{abs} in ApJ Table 6 are too small by a factor of 1.086 .

band	λ (μm)	albedo	$g \equiv \langle \cos \theta \rangle$ ^b	Σ_{ext} ^c ($\text{cm}^2 \text{ H}^{-1}$)	κ_{abs} ^d ($\text{cm}^2 \text{ g}^{-1}$)
Ly edge	0.0100	0.47	1.00	7.11×10^{-22}	2.00×10^4
	0.0488	0.30	0.86	1.52×10^{-21}	5.66×10^4
	0.0912	0.24	0.73	2.51×10^{-21}	1.01×10^5
	0.100	0.27	0.72	2.28×10^{-21}	8.83×10^4
Ly α	0.1215	0.32	0.73	1.73×10^{-21}	6.20×10^4
	0.150	0.38	0.70	1.38×10^{-21}	4.56×10^4
	0.220	0.42	0.56	1.65×10^{-21}	5.05×10^4
	0.300	0.58	0.57	1.00×10^{-21}	2.25×10^4
U	0.365	0.62	0.58	8.28×10^{-22}	1.68×10^4
B	0.440	0.65	0.57	6.73×10^{-22}	1.26×10^4
V	0.550	0.67	0.54	5.06×10^{-22}	8960
R	0.700	0.66	0.48	3.59×10^{-22}	6460
I	0.900	0.63	0.40	2.47×10^{-22}	4820
J	1.22	0.58	0.29	1.53×10^{-22}	3440
H	1.63	0.51	0.21	9.76×10^{-23}	2510
K	2.20	0.43	0.13	5.92×10^{-23}	1780
L	3.45	0.28	0.0051	2.57×10^{-23}	984
	3.60	0.26	-0.0037	2.37×10^{-23}	926
	4.50	0.18	-0.037	1.54×10^{-23}	670
	4.80	0.16	-0.043	1.37×10^{-23}	611
M	5.80	0.099	-0.052	1.02×10^{-23}	488
	8.00	0.016	-0.050	1.54×10^{-23}	803
	9.70	0.003	-0.036	4.39×10^{-23}	2320
	10.6	0.003	-0.032	3.36×10^{-23}	1770
N	12.0	0.003	-0.029	1.93×10^{-23}	1020
	21.0	5×10^{-4}	-0.024	1.30×10^{-23}	693
	25.0	3×10^{-4}	-0.024	9.29×10^{-24}	493
	60.0	1×10^{-4}	< 0.01	1.91×10^{-24}	101
Q	70.0	1×10^{-4}	< 0.01	1.38×10^{-24}	73.1
	100	< 10^{-4}	< 0.01	6.40×10^{-25}	34.0
	140	< 10^{-4}	< 0.01	3.31×10^{-25}	17.6
	160	< 10^{-4}	< 0.01	2.44×10^{-25}	13.0
	240	< 10^{-4}	< 0.01	1.06×10^{-25}	5.61
	450	< 10^{-4}	< 0.01	2.80×10^{-26}	1.49
	850	< 10^{-4}	< 0.01	8.83×10^{-27}	0.468
	1350	< 10^{-4}	< 0.01	4.05×10^{-27}	0.215
	2000	< 10^{-4}	< 0.01	2.10×10^{-27}	0.111
	3000	< 10^{-4}	< 0.01	1.05×10^{-27}	0.0559

^aAn expanded version of this table is available at <http://www.astro.princeton.edu/~draine/dust/dustmix.html>

^bAverage of $\cos \theta$ for scattered light, where θ is the scattering angle.

^c Σ_{ext} is the dust extinction cross section per H nucleon.

^d κ_{abs} is the absorption opacity of the dust alone; the opacity of the gas+dust mixture is $\kappa_{\text{abs}}/125$. To within $\pm 10\%$, $\kappa_{\text{abs}} \approx 3.17 \times 10^5 (\lambda/\mu\text{m})^{-2} (\text{cm}^2 \text{ g}^{-1})$ for $20 < \lambda < 700 \mu\text{m}$, and $\kappa_{\text{abs}} \approx 3.89 \times 10^4 (\lambda/\mu\text{m})^{-1.68} \text{ cm}^2 \text{ g}^{-1}$ for $700 < \lambda < 10^4 \mu\text{m}$.

7.7, 8.6, and 11.3 μ m features are hidden by the much stronger 9.7 μ m silicate feature, and therefore will be difficult to observe as absorption features.

The aromatic absorption bands allow us to place constraints on the PAH abundance if the PAH band strengths are known. On the other hand, one can also infer information on the PAH band strengths from the aromatic absorption bands given knowledge of the PAH abundance derived from other considerations such as the 2175Å hump and/or the 3–12 μ m PAH emission bands. For example, for $b_C=60$ ppm in PAHs (the maximum allowed by the 2175Å hump), and assuming $a_\xi \approx 50$ Å, enhancement of the 6.2 μ m band by a factor $E_{6.2} > 3$ would result in a 6.2 μ m absorption feature which would be stronger than observed; conversely, if we had not enhanced the 6.2 μ m feature strength by a factor $E_{6.2}=3$, then the 6.2 μ m absorption feature strength in the model would be weaker than observed. However, this depends on the poorly-constrained value of a_ξ , which determines the radius where carbonaceous grains make the transition from being PAH-like to becoming graphite-like. It is clear that $(\int \Delta\tau d\lambda^{-1})_{6.2}$ would increase (decrease) as a_ξ is increased (decreased) (e.g., the $a_\xi = 100$ Å model results in $(\int \Delta\tau d\lambda^{-1})_{6.2}/\Delta\tau_{9.7} \approx 4.2 \text{ cm}^{-1}$). Therefore, until we have better understanding of the PAH-graphite transition, we should not over-state the constraints of the aromatic absorption bands on the PAH band strengths. However, the fact that our model is consistent with the 3.3, 6.2 μ m absorption bands, the 2175Å hump, and the 3–12 μ m emission indicates that the choice of $a_\xi=50$ Å is reasonable.

We must also stress that the strengths of these PAH absorption bands could vary with physical conditions due to changes in the PAH ion fraction $\phi_{\text{ion}}(a)$. In regions with increased ϕ_{ion} , the 6.2 μ m absorption feature would be strengthened and the 3.3 μ m feature would be weakened (see Table 1). The fact that there is no significant variation between the Galactic center sources and the local sources for the 6.2 μ m absorption strength relative to the silicate optical depth (Schutte et al. 1998) suggests that these regions probably have similar radiation field-to-electron density ratios. This is also indicated by the $P(7.7\mu\text{m})/P(11.3\mu\text{m})$ data of Chan et al. (2001) (see their Figure 2c).

Significant variations in the relative abundances of PAHs to large grains are expected in different environments due to depletion (e.g., accretion of PAHs into grain mantles, agglomeration of PAHs and other very small grains to form composite grains), production (e.g. fragmentation of graphitic grains, hydrogenated amorphous carbon [Scott, Duley, & Pinho 1997] or organic refractory materials [Greenberg et al. 2000]), or drift of large grains relative to small grains due to anisotropic starlight (Weingartner & Draine 2001c). Such local variations in PAH abundance are indicated by the large cloud-to-cloud variations in mid-IR emission (Verter et al. 2000) as well as the lower UV extinction in dense regions.

Ultrasmall silicate grains are excluded as a major component since the IRTS and ISO spectroscopic observations of the diffuse ISM show no evidence of the Si-O 9.7 μ m emission feature which would be expected for transiently-heated tiny silicate dust (Mattila et al. 1996; Onaka et al. 1996). However, the presence of these particles cannot be ruled out since a weak 9.7 μ m emission feature may be hidden by the strong PAH features at 8.6 μ m and 11.3 μ m. On the basis of the observed IR emission spectrum for the diffuse ISM, the observed ultraviolet extinction curve, and the 10 μ m silicate absorption profile, Li & Draine (2001) have obtained upper limits on the abundances of ultrasmall ($a \lesssim 15$ Å) amorphous and crystalline silicate grains. It is found that, contrary to previous work ($\lesssim 1\%$ of solar silicon abundance [Désert et al. 1986]), as much as $\sim 10\%$ of interstellar Si could be in $a \lesssim 15$ Å silicate grains without violating observational constraints. Not more than $\sim 5\%$ of the Si can be in crystalline silicates (of any size).

12. Summary

We have modeled the infrared emission spectra from dust in the diffuse ISM of the Milky Way, including the prominent emission features at 3.3, 6.2, 7.7, 8.6 and $11.3\mu\text{m}$ and the continuum emission from near-IR to submillimeter. We have compared our model to the observed emission from high galactic latitude regions as well as from regions in the Galactic plane.

The dust model adopted here consists of a mixture of amorphous silicate grains and carbonaceous grains, both having a wide size distribution ranging from large grains $\sim 1\mu\text{m}$ in diameter, down to molecules containing tens of atoms. We assume that the carbonaceous grains have graphitic properties at radii $a \gtrsim 50\text{\AA}$, and polycyclic aromatic hydrocarbon (PAH)-like properties at the very small sizes (see §2.2) which account for the 3.3, 6.2, 7.7, 8.6 and $11.3\mu\text{m}$ emission features seen in a wide range of objects.

Based on recent progress made in both laboratory and theoretical studies of PAH absorption spectra, and guided by the astronomical observations, we have constructed “astronomical” absorption cross sections for both neutral and ionized PAHs from the far ultraviolet to the infrared (see §2.3, Table 1, and Appendix A) including dependence on grain size (which affects the onset of the absorption edge at long wavelength [see §A.2]), H/C ratio, and charge state. Detailed modelling indicates that the feature strengths of the 7.7, $8.6\mu\text{m}$ bands need to be increased by a factor ~ 2 , and a factor ~ 3 for the $6.2\mu\text{m}$ band (see §2.3 and compare Figures 10a and 14a). In addition, a small amount of continuum absorption needs to be added to the PAH absorption spectrum to account for the near-IR continuum emission at $1\text{--}5\mu\text{m}$ underlying the $3.3\mu\text{m}$ C-H stretching feature detected in various sources (see §2.4). We represent this continuum opacity by adding about 1% of the opacity of graphite. We have also slightly modified the far-infrared and submillimeter emissivity of “astronomical silicate” in order to explicitly demonstrate that the observed emission from the interstellar medium can be reproduced using reasonable properties for carbonaceous and silicate grains.

We model the heat capacities of carbonaceous and silicate grains using vibrational models developed by DL01. The thermal-discrete method developed in DL01 is used to calculate the energy (temperature) distribution functions for transiently heated very small grains (see §6). We find that for grains heated by starlight with $\chi_{\text{MMP}} = 1$, the energy distribution function is quite broad even for grains as large as $a = 200\text{\AA}$, resulting in stronger emission at short wavelengths than would be computed using the “equilibrium temperature” \bar{T} . The PAH charging computation is performed using the technique developed by Weingartner & Draine (2001b) (see §8).

We adopt the size distributions for large grains (see §7) derived from modeling the interstellar extinction curve (Weingartner & Draine 2001a). We find that if the very small carbonaceous grain population includes two log-normal size distributions characterized by $a_{01} = 3.5\text{\AA}$, $a_{02} = 30\text{\AA}$, and widths $\sigma = 0.4$ for the PAH size distributions (with about 60ppm of C [relative to H] contained in PAHs; 45ppm in the former, and 15ppm in the latter), then the overall grain model is able to closely reproduce the observed emission of the diffuse ISM from near-IR to submillimeter (see §10) while at the same time reproducing the observed extinction curve. Our dust model predicts a pronounced absorption feature at $6.2\mu\text{m}$ and a much weaker feature at $3.3\mu\text{m}$ due to PAHs with optical depths consistent with observations (see §11).

We will show elsewhere (Draine & Li 2000b) that the very same ultrasmall grain component (i.e. PAHs) invoked here to account for the $3\text{--}60\mu\text{m}$ *vibrational* emission will produce “*rotational*” emission which can quite naturally explain the observed 10–100GHz “anomalous” microwave emission from the interstellar medium, confirming the original estimates by Draine & Lazarian (1998a,b).

While real interstellar grains are no doubt more complex than the simple model presented here, this

extension of the original graphite-silicate grain model (Mathis, Rumpl, & Nordsieck 1977; Draine & Lee 1984) to explicitly include a PAH population leads to a well-defined grain model which is in excellent agreement with available observational constraints, ranging from the observed extinction curve to the observed infrared emission.

We thank L.J. Allamandola, R. Arendt, J.M. Greenberg, and J.C. Weingartner for helpful discussions. We are grateful to the anonymous referee for helpful comments. We thank D.M. Hudgins and L.J. Allamandola for providing us with access to their PAH database. We thank F. Boulanger, D. Cesarsky, E. Sturm, K.I. Uchida, and L. Verstraete for providing us with observational data. We thank D.P. Finkbeiner and D.J. Schlegel for help in obtaining the DIRBE fluxes for regions in the Galactic plane. We thank R.H. Lupton for the availability of the SM plotting package. This research was supported in part by NASA grant NAG5-7030 and NSF grants AST-9619429 and AST-9988126.

A. Optical Properties of Polycyclic Aromatic Hydrocarbons

A.1. The UV and Far-UV Range

Donn (1968) originally proposed that PAHs could contribute significantly to the interstellar UV extinction. Although a single PAH species has strong UV absorption features (UV Atlas 1966), a cosmic mixture of many individual molecules, radicals, and ions, with many overlapping absorption bands, may effectively produce an absorption continuum, except perhaps in the visible, where some narrow features may stand out and account for some of the diffuse interstellar bands, and in the 2000–2400Å region, where a concentration of strong absorption features may blend together to produce the 2175Å extinction feature.

Efforts over the past two decades to measure the absorption spectrum of PAHs have been primarily for individual ionized/neutral PAH molecules in hopes of identifying carriers of the diffuse interstellar bands (see Salama et al. 1996 and references therein). To the best of our knowledge, the only high quality absorption spectra published for natural mixtures of PAHs from the visible to far-UV are those of Léger et al. (1989b) and Joblin et al. (1992). For $3.3 \mu\text{m}^{-1} < \lambda^{-1} < 10 \mu\text{m}^{-1}$, we adopt their experimental spectra as a starting point. All these spectra have a strong UV feature around 2175Å (but relatively broader than the interstellar feature). We use the method of Fitzpatrick & Massa (1990) to fit the *averaged* spectra of Léger et al. (1989b)⁹ and of Joblin et al. (1992)¹⁰ by a Drude profile plus a linear continuum and a nonlinear far-ultraviolet ($\lambda^{-1} > 5.9 \mu\text{m}^{-1}$) rise. To be consistent with the observed extinction, we then adjust the peak position of the near-UV hump (due to the π - π^* transition) to be at $\lambda_{\pi-\pi^*}^{-1} = 4.6 \mu\text{m}^{-1}$ and the band width FWHM to be $\gamma\lambda_{\pi-\pi^*}^{-1} = 1.0 \mu\text{m}^{-1}$, with the integrated cross section conserved.¹¹ We thus obtain eq. (10),

⁹We adopted the PAH mixtures obtained from a coal pitch extract evaporated at 380K (averaged over those of 381K and 385K), 410K, 440K (averaged over 436K and 440K), and 476K. In these mixtures over 300 molecules were identified with molecular mass ranging from $\sim 150 - 350$ amu. The measurements were performed only for $\lambda^{-1} < 7.7 \mu\text{m}^{-1}$, beyond which extrapolations were made.

¹⁰These mixtures were from a coal pitch extract evaporated at 570K, 600K and 630K, with molecular masses ranging from 170 to 550 amu.

¹¹The carrier of the 2175Å extinction hump remains unidentified more than 35 years after its first detection (Stecher 1965). It is commonly attributed to some sort of graphitic carbonaceous material (see Draine 1989a). A correlation between the 2175Å hump and the IRAS 12μm emission (dominated by PAHs) was found by Boulanger, Prévot, & Gry (1994) in the Chamaeleon cloud, suggesting a common carrier. Arguments against PAHs as the 2175Å hump carrier can be found in Mathis (1998) where

for $3.3 < \lambda^{-1} < 5.9 \mu\text{m}^{-1}$.

For $\lambda^{-1} > 10 \mu\text{m}^{-1}$, no experimental data for PAH mixtures are available. We adopt that of coronene $\text{C}_{24}\text{H}_{12}$, characterized by a strong increase with λ^{-1} out to a strong peak at $\approx 700\text{\AA}$ (due to the σ - σ^* transition). Other simpler aromatic molecules such as naphthalene (C_{10}H_8) (Koch, Otto, & Radler 1972), benzene (C_6H_6) and its derivatives (Robin 1975) display similar spectral behaviour in the range of 10–30eV. For $10 \mu\text{m}^{-1} < \lambda^{-1} < 15 \mu\text{m}^{-1}$, the laboratory measurements of coronene (Léger et al. 1989b) are fitted by a Drude profile plus a linear continuum to obtain eq. (7).

For $\lambda^{-1} > 17.25 \mu\text{m}^{-1}$, we adopt the absorption cross sections per C atom calculated from the refractive indices of graphite (DL84); see eq. (5). A smooth transition from the absorption spectrum of coronene to that of graphite is made by extrapolating the coronene data to $\lambda^{-1} \approx 17.25 \mu\text{m}^{-1}$, resulting in eq. (6).

To smoothly join our eq. (7) for $\lambda^{-1} > 10 \mu\text{m}^{-1}$ to eq. (9) for $\lambda^{-1} < 7.7 \mu\text{m}^{-1}$, for $7.7 < \lambda^{-1} < 10 \mu\text{m}^{-1}$ we adopt the polynomial eq.(8), which provides a good fit to the experimental data for PAH mixtures.

A.2. The Visible and Near-UV Range

The visible and near UV absorption properties of PAHs have been extensively studied (Clar 1964; Salama et al. 1996 and references therein). However, there are no high quality absorption spectra for PAH mixtures available in the literature. Therefore we adopt that of circumanthracene ($\text{C}_{40}\text{H}_{16}$), the largest symmetric PAH with the visible and near UV spectrum measured to date. The laboratory absorption spectrum of circumanthracene (Clar 1964) can be approximated by

$$[C_{\text{abs}}(\lambda)/N_{\text{C}}]_{\text{C}_{40}\text{H}_{16}} = 2.54 \times 10^{-17-3.431(\lambda/\mu\text{m})} \text{ cm}^2/\text{C}. \quad (\text{A1})$$

We adopt the cutoff function of Désert et al. (1990),

$$\text{cutoff}(\lambda, \lambda_c) = \frac{1}{\pi} \arctan \left[\frac{10^3(y-1)^3}{y} \right] + \frac{1}{2}, \quad y = \lambda_c/\lambda, \quad (\text{A2})$$

where the cutoff wavelength λ_c – the visual absorption edge – is derived from the extensive discussion of Salama et al. (1996):

$$\left[\frac{\lambda_c}{\mu\text{m}} \right] = \begin{cases} 1/(3.804M^{-0.5} + 1.052), & \text{for neutral PAHs;} \\ 1/(2.282M^{-0.5} + 0.889), & \text{for PAH cations;} \end{cases} \quad (\text{A3})$$

where M , the number of fused benzenoid rings, is approximately $M \approx 0.4N_{\text{C}}$ for $N_{\text{C}} > 40$, $M \approx 0.3N_{\text{C}}$ for $N_{\text{C}} < 40$ (N_{C} is the number of carbon atoms). Upon ionization, the visual absorption edge λ_c shifts to longer wavelength; λ_c also shifts to longer wavelength as the PAH size increases.

To smoothly join the visual-near UV spectrum with that of $\lambda^{-1} > 3.3 \mu\text{m}^{-1}$ (§A.1), we multiply the absorption cross section (A1) of circumanthracene by a factor 1.36, to obtain eq. (11) for $1 \lesssim \lambda^{-1} \lesssim 3.3 \mu\text{m}^{-1}$.

it was argued that the hump peak is sensitive to the PAH shape (but also see Duley & Seahra 1998) and the hump strength is sensitive to the states of ionization (e.g. Lee & Wdowiak [1993] found that the 2175Å hump is weakened in cations). In the dust model presented here the both the 2175Å extinction hump and the 12μm emission are mainly contributed by PAHs, but we note that PAHs are not the major contributor to the far-UV ($\lambda < 1800\text{\AA}$) extinction. This is consistent with the observation that the far-UV extinction does not correlate with either the 2175Å hump (Greenberg & Chlewicki 1983) or the IRAS 12μm emission (Boulanger et al. 1994).

Table 7. Observed PAH band widths (FWHM, μm) in selected sources.

Objects	3.3 μm	6.2 μm	7.7 μm	8.6 μm	11.3 μm	11.9 μm	12.7 μm	Reported res.	Method ^a	Spectrum sources
diffuse ISM	0.20 ^b	0.67	0.91	0.55	0.63	-	-	$\Delta\lambda = 0.3\mu\text{m}$	Drude	Onaka et al. 1996
vdB 133 (little UV flux)	-	0.30	0.78	0.50	0.60	-	0.85	$\lambda/\Delta\lambda = 40$	Drude	Uchida et al. 1998
M17 (PDR)	-	0.30	0.68	0.42	0.60	-	0.80	$\lambda/\Delta\lambda = 40$	Drude	Cesarsky et al. 1996a
NGC 7023 (reflection nebula)	0.04 ^c	0.28	0.60	0.42	0.43	-	0.80	$\lambda/\Delta\lambda = 40$	Drude	Cesarsky et al. 1996b
NGC 7023 (reflection nebula)	0.04 ^c	0.17	0.72	0.28	0.22	-	0.33	$\lambda/\Delta\lambda = 500$	Eye	Moutou et al. 1999b
NGC 1333 (reflection nebula) ^d	0.04 ^e	0.35	0.70	0.43	0.40 ^f	-	-	$\lambda/\Delta\lambda = 40$	Lorentzian	Uchida et al. 2000
ρ Oph (molecular cloud)	-	0.27	0.70	0.42	0.43	-	1.18	$\lambda/\Delta\lambda = 40$	Lorentzian	Boulanger et al. 1996
SMC	-	0.20	0.53	0.36	0.54	-	-	$\lambda/\Delta\lambda = 40$	Lorentzian	Reach et al. 2000
Diffuse ISM	-	0.20	0.71	0.42	0.27	-	-	$\Delta\lambda = 0.1\mu\text{m}$	Cauchy	Mattila et al. 1996
NGC 891 (external galaxy)	-	0.22	0.62	0.30	0.30	-	-	$\Delta\lambda = 0.1\mu\text{m}$	Cauchy	Mattila et al. 1999
28 normal galaxies (averaged)	-	0.36	0.77	0.45	0.42	-	-	$\Delta\lambda = 0.1\mu\text{m}$	Drude	Helou et al. 2000
Orion ionization front	0.04 ^g	0.24 ^h	0.80 ^h	0.28 ^h	0.14	-	0.27	$\Delta\lambda = 0.09\mu\text{m}$	Gaussian	Roche et al. 1989
NGC 2023 (reflection nebula)	0.04 ^e	0.20	0.74	0.38	0.36	-	-	$\lambda/\Delta\lambda = 500$	Drude	Verstraete et al. 2001
Red Rectangle (post-AGB)	0.035 ^g	0.16	0.65	0.36	0.21	0.30	0.42	$\lambda/\Delta\lambda \approx 1000$	Eye	Tielens et al. 1999
30 Dor (LMC) ⁱ	0.036	0.30	0.60	0.40	0.20	-	-	$\lambda/\Delta\lambda = 1500$	Drude	Sturm et al. 2000
M82 (starburst galaxy)	0.04	0.20	0.71	0.42	0.19	-	-	$\lambda/\Delta\lambda = 1500$	Drude	Sturm et al. 2000
NGC 253 (starburst galaxy)	0.042	0.18	0.78	0.45	0.19	-	-	$\lambda/\Delta\lambda = 1500$	Drude	Sturm et al. 2000
Circinus(Seyfert 2 galaxy)	0.045	0.16	0.82	0.43	0.20	-	-	$\lambda/\Delta\lambda = 1500$	Drude	Sturm et al. 2000
Present Model	0.04 ^j	0.20	0.70	0.40	0.20 ^k	0.30	0.30 ^k	-	-	this work

^aFWHM values are determined by fitting the PAH features either with a set of Drude profiles, or Cauchy, Gaussian, Lorentzian profiles, or simply estimated by reading off the source spectra (hereafter “Eye”); those marked with “Cauchy”, “Gaussian”, or “Lorentzian” are taken from the source references; those marked with “Drude” or “Eye” are obtained in this work.

^bTanaka et al. 1996 (resolution $\Delta\lambda = 0.13\mu\text{m}$).

^cMoutou et al. 1999a (resolution $\lambda/\Delta\lambda = 500$).

^dUchida et al. (2000) have shown that the FWHM of the 6.2, 7.7, 8.6 μm bands remains constant over different nebular positions with $G_0 \gtrsim 200$; however, the 7.7 μm band appears to be broader at low G_0 .

^eJoblin et al. 1996a (resolution $\Delta\lambda = 0.008\mu\text{m}$).

^fJoblin et al. 1996b (resolution $\lambda/\Delta\lambda = 60$).

^gGeballe et al. 1989 (resolution $\Delta\lambda = 0.009\mu\text{m}$).

^hBregman et al. 1989 (resolution $\Delta\lambda = 0.12\mu\text{m}$).

ⁱExcept the 3.3 and 11.3 μm bands, the signal-to-noise ratio is very low for the 30 Dor spectrum (Sturm et al. 2000).

^jIn a high resolution ($\lambda/\Delta\lambda \approx 1400$) survey of eight sources, Tokunaga et al. (1991) found that the 3.3 μm feature in extended objects such as planetary nebulae and HII regions has a band width of $\approx 0.042\mu\text{m}$; this was further confirmed by Roche et al. (1996) who found 18 planetary nebulae all have a band width of $\approx 0.04\mu\text{m}$ for the 3.3 μm feature ($\lambda/\Delta\lambda = 500$).

^kOn average, the 10–15 μm spectra of 16 HII regions, YSOs, and evolved stars (with resolution $\lambda/\Delta\lambda = 500 - 1500$) show a band width of $\approx 0.20, 0.29\mu\text{m}$ for the 11.3, 12.7 μm band, respectively (see Hony et al. 2001).

A.3. The Near-IR, Mid-IR Range

During the last few years, a great deal of progress has been made by experimentalists and theorists in the study of the infrared properties of both neutral and ionized PAHs (Allamandola et al. 1999a; Hudgins & Allamandola 1999a, 1999b; Langhoff 1996; and references therein). The infrared spectra of PAHs are characterized by the C-C and C-H stretching/bending vibrational features. Observationally, the feature positions and widths are approximately constant in a wide variety of objects. Table 7 summarizes the band widths of the major PAH features observed in some well-observed astronomical sources. We represent the PAH infrared absorption (actually emission) cross sections by a set of Drude profiles with peak wavelengths λ_j and FWHM $\gamma_j \lambda_j$ taken from the observations¹² (see Table 7), respectively. Although the laboratory spectra of various PAH species are not exactly at the same wavelengths as the astronomical observations, we note that large symmetric compact PAHs are in close agreement with interstellar observations (see Langhoff 1996).

Although weaker than the $11.3\mu\text{m}$ resonance, other C-H out-of-plane (oop) bending modes¹³, have also been detected in various regions (Witteborn et al. 1989; Hony et al. 2001). From the point of view of stability, compact, symmetric structures are favored for interstellar PAHs (van der Zwet & Allamandola 1985; Omont 1986; Allamandola et al. 1989; Jochims et al. 1994). Thus one expects a much lower quartet-CH ($13.6\mu\text{m}$) abundance than solo-, duet-, and trio-CH for interstellar PAHs, as has been recently confirmed by ISO observations (Hony et al. 2001). For large symmetric compact PAHs, it is reasonable to assume equal single, double, and triple adjacent CH units (Stein & Brown 1991). We therefore include Drude profiles with central wavelengths $\lambda_j = 11.9, 12.7\mu\text{m}$ and FWHM $\gamma_j \lambda_j = 0.30, 0.30\mu\text{m}$ in our PAH model spectrum for the duet-CH, trio-CH out-of-plane bending modes, respectively.

Based on recent laboratory and theoretical studies of neutral and ionized PAHs (deFrees et al. 1993; Szczepanski & Vala 1993; Hudgins, Allamandola, & Sandford 1994; Hudgins & Allamandola 1995a, 1995b, 1997; Langhoff 1996; Pauzat, Talbi, & Ellinger 1997; Hudgins & Sandford 1998a, 1998b, 1998c) we estimate the integrated cross section of the C-C, C-H bands for neutral PAHs and PAH cations (normalized by the number of C atoms for C-C modes and by the number of H atoms for C-H modes). The results are presented in Table 1. We have considered only two charge states – neutral PAHs and PAH cations – since no experimental measurements have been made for multiply-ionized PAHs. It has been shown that the IR properties of PAH anions closely resemble those of PAH cations (e.g., see Szczepanski, Wehlburg, & Vala 1995; Langhoff 1996; Hudgins et al. 2000) except for the very strong $3.3\mu\text{m}$ C-H stretch enhancement in the anion¹⁴.

¹²We rely on the highest resolution observations to indicate the FWHM of the narrower PAH features.

¹³The C-H oop bending modes are characteristic of the edge structure of PAHs. They occur at different wavelengths, depending on the number of neighbouring hydrogen atoms on one aromatic ring: for neutral PAHs, isolated C-H oop band (solo-CH) occurs at $\sim 11.3\mu\text{m}$, doubly adjacent CH (duet-CH) at $\sim 11.9\mu\text{m}$, triply adjacent CH (trio-CH) at $\sim 12.7\mu\text{m}$, quadruply adjacent CH at $\sim 13.6\mu\text{m}$. Upon ionization, the solo and duet CH modes shift to shorter wavelength (see Hudgins & Allamandola 1999b).

¹⁴The $3.3\mu\text{m}$ C-H stretching mode is about 3 times more intense in anions than the corresponding mode in neutral PAHs; however, no cation features have been observed in this mode (Hudgins et al. 2000).

A.4. The Far-IR Range

The far-IR properties of PAHs are poorly known. Moutou et al. (1996) have carried out measurements of 40 PAH species in the range of 14–75 μm . They found four prominent features at 16.2, 18.3, 21.2 and 23.1 μm (with band widths FWHM = 10, 20, 18, 20 cm^{-1} , respectively) and a weak continuum beyond 40 μm ¹⁵. To include these far-IR features, we adopt 4 Drude profiles for the 16.4, 18.3, 21.2 and 23.1 μm bands and one Drude profile for the far-IR continuum ($\lambda > 24 \mu\text{m}$). Band widths are taken from Moutou et al. (1996) except for the 16.4 μm feature, for which we adopt $\sim 0.16 \mu\text{m}$ (Moutou et al. 2000). The integrated band strengths for the 16.4, 18.3, 21.2, and 23.1 μm bands were estimated from the 40 species in Table 3 of Moutou et al. (1996) by (1) summing the band strengths per C atom of features within $\pm 20 \text{ cm}^{-1}$ of the nominal band centers, (2) dividing by 40, and (3) multiplying the resulting band strength per C atoms by a factor of 2 (a) since many of the species studied by Moutou et al. (e.g., hexabenzocoronene $\text{C}_{42}\text{H}_{18}$) are highly symmetric and show only weak absorption in the 14–40 μm region and (b) in order to reproduce the observed strength of the 16.4 μm feature relative to shorter wavelength features (e.g., 11.3 μm) in the spectrum of NGC 7023 (Moutou et al. 1999a).

The parameters for the FIR continuum Drude profile ($\sigma_{\text{int},14}$, λ_{14} , γ_{14} ; see Table 1) were chosen by setting $\sigma_{\text{int},14} \approx \int_{14 \mu\text{m}}^{\infty} N_{\text{C}}^{-1} C_{\text{abs}}^{\text{PAH}}(\lambda) d\lambda^{-1} - \sum_{j=10}^{13} \sigma_{\text{int},j}$ averaged over the laboratory spectra of 40 PAH species (Moutou et al. 1996), and choosing λ_{14} , γ_{14} to (1) minimize effects on the near-IR ($\lambda < 14 \mu\text{m}$) spectrum; (2) avoid a noticeable hump in the far infrared ($\lambda > 24 \mu\text{m}$) spectrum; (3) minimize absorption at $\lambda > \lambda_{\text{max}}$, where λ_{max} corresponds to the lowest vibrational mode (see DL01); (4) have the far infrared continuum dropping approximately as $\propto \lambda^{-2}$ for $\lambda > 24 \mu\text{m}$.

REFERENCES

- Agladze, N.I., Sievers, A.J., Jones, S.A., Burlitch, J.M., & Beckwith, S.V.W. 1996, *ApJ*, 462, 1026
- Allain, T., Leach, S., & Sedlmayr, E. 1996, *A&A*, 305, 602
- Allamandola, L.J., Tielens, A.G.G.M., & Barker, J.R. 1985, *ApJ*, 290, L25
- Allamandola, L.J., Tielens, A.G.G.M., & Barker, J.R. 1989, *ApJS*, 71, 733
- Allamandola, L.J., Hudgins, D.M., & Sandford, S.A. 1999a, *ApJ*, 511, L115
- Allamandola, L.J., Hudgins, D.M., Bauschlicher, C.W., Jr., & Langhoff, S.R. 1999b, *A&A*, 352, 659
- Arendt, R.G., Odegard, N., Weiland, J.L., et al. 1998, *ApJ*, 508, 74
- Bakes, E.L.O., & Tielens, A.G.G.M. 1994, *ApJ*, 427, 822
- Barker, J.R., & Cherchneff, I. 1989, in *Interstellar Dust* (IAU Symposium 135), ed. L.J. Allamandola & A.G.G.M. Tielens (Dordrecht: Kluwer), 197
- Bernstein, M.P., Sandford, S.A., & Allamandola, L.J. 1996, *ApJ*, 472, L127

¹⁵A 16.4 μm emission feature was detected in the ISO-SWS spectra of NGC 7023, M17 and the Orion Bar by Moutou et al. (2000). Therefore we adopt 16.4 μm rather than 16.2 μm .

- Bohren, C.F., & Huffman, D.R. 1983, *Absorption and Scattering of Light by Small Particles* (New York: Wiley)
- Borghesi, A., Bussolletti, E., & Colangeli, L. 1987, *ApJ*, 314, 422
- Boulanger, F. 1999, in *Solid Interstellar Matter: The ISO Revolution*, ed. L. d'Hendecourt, C. Joblin & A. Jones (New York: Springer), 19
- Boulanger, F., Baud, B., & van Albada, G.D. 1985, *A&A*, 144, L9
- Boulanger, F., Boissel, P., Cesarsky, D., & Ryter, C. 1998, *A&A*, 339, 194
- Boulanger, F., & Pérault, M. 1988, *ApJ*, 330, 964
- Boulanger, F., Prévot, M. L., & Gry, C. 1994, *A&A*, 284, 956
- Bregman, J.D., Allamandola, L.J., Witteborn, F.C., Tielens, A.G.G.M., & Geballe, T.R. 1989, *ApJ*, 344, 791
- Brenner, J.D., & Barker, J.R. 1992, *ApJ*, 388, L39
- Brooke, T.Y., Sellgren, K., & Geballe, T.R. 1999, *ApJ*, 517, 883
- Cardelli, J.A., Clayton, G.C., & Mathis, J.S. 1989, *ApJ*, 467, 334
- Cesarsky, D., Lequeux, J., Abergel, A., et al. 1996a, *A&A*, 315, L309
- Cesarsky, D., Lequeux, J., Abergel, A., et al. 1996b, *A&A*, 315, L305
- Chan, K.-W., Roellig, T.L., Onaka, T., et al. 2001, *ApJ*, 546, 273
- Cherchneff, I., & Barker, J.R. 1989, *ApJ*, 341, L21
- Chiar, J.E., Tielens, A.G.G.M., Whittet, D.C.B., et al. 2000, *ApJ*, 537, 749
- Clar, E. 1964, *Polycyclic Hydrocarbons* (New York: Academic Press)
- Cohen, M., Tielens, A.G.G.M., Bregman, J., et al. 1989, *ApJ*, 341, 246
- Cook, D.J., Schlemmer, S., Balucani, N., et al. 1998, *J. Phys. Chem.*, 102, 1465
- de Frees, D.J., Miller, M.D., Talbi, D., Pauzat, F., & Ellinger, Y. 1993, *ApJ*, 408, 530
- Désert, F.X., Boulanger, F., Léger, A., et al. 1986, *A&A*, 159, 328
- Désert, F.X., Boulanger, F., & Puget, J.L. 1990, *A&A*, 237, 215
- d'Hendecourt, L.B., Léger, A., Boissel, P., & Désert, F.X. 1989, in *Interstellar Dust (IAU Symposium 135)*, ed. L.J. Allamandola & A.G.G.M. Tielens (Dordrecht: Kluwer), 207
- Donn, B. 1968, *ApJ*, 152, L129
- Draine, B.T. 1984, *ApJ*, 277, L71
- Draine, B.T. 1989a, in *Interstellar Dust (IAU Symposium 135)*, ed. L.J. Allamandola & A.G.G.M. Tielens (Dordrecht: Kluwer), 313

- Draine, B.T. 1989b, in *Infrared Spectroscopy in Astronomy*, Proc. 22nd Esrlab Symposium, ed. B.H. Kaldeich, 93
- Draine, B.T., & Anderson, N. 1985, *ApJ*, 292, 494
- Draine, B.T., & Lazarian, A. 1998a, *ApJ*, 494, L19
- Draine, B.T., & Lazarian, A. 1998b, *ApJ*, 508, 157
- Draine, B.T., & Lee, H.M. 1984, *ApJ*, 285, 89 (DL84)
- Draine, B.T., & Li, A. 2001, *ApJ*, 551, 807
- Draine, B.T., & Malhotra, S. 1993, *ApJ*, 414, 632
- Draine, B.T., & Sutin, B. 1987, *ApJ*, 320, 803
- Duley, W.W., & Seahra, S. 1998, *ApJ*, 507, 874
- Duley, W.W., & Williams, D.A. 1981, *MNRAS*, 196, 269
- Duley, W.W., Jones, A.P., & Williams, D.A. 1989, *MNRAS*, 236, 709
- Dwek, E. 1997, *ApJ*, 484, 779
- Dwek, E., Arendt, R.G., Fixsen, D.J., et al. 1997, *ApJ*, 475, 565
- Finkbeiner, D.P., Davis, M., & Schlegel, D.J. 1999, *ApJ*, 524, 867
- Fitzpatrick, E.L. 1999, *PASP*, 111, 63
- Fitzpatrick, E.L., & Massa, D. 1990, *ApJS*, 72, 163
- Geballe, T.R., Tielens, A.G.G.M., Allamandola, L.J., Moorhouse, A., & Brand, P.W.J.L. 1989, *ApJ*, 341, 278
- Gillett, F.C., Forrest, W.J., & Merrill, K.M. 1973, *ApJ*, 184, L93
- Greenberg, J.M. 1960, *ApJ*, 132, 672
- Greenberg, J.M. 1968, in *Stars and Stellar Systems*, Vol. VII, ed. B.M. Middlehurst & L.H. Aller (Chicago: Univ. of Chicago Press), 221
- Greenberg, J.M. 1978, in *Cosmic Dust*, ed. J.A.M. McDonnell (New York: Wiley), 187
- Greenberg, J.M., & Chlewicki, G. 1983, *ApJ*, 272, 563
- Greenberg, J.M., Gillette, J.S., Muñoz Caro, G.M., et al. 2000, *ApJ*, 531, L71
- Guhathakurta, P., & Draine, B. T. 1989, *ApJ*, 345, 230
- Habing, H.J. 1968, *Bull. Astron. Inst. Netherlands*, 19, 421
- Hauser, M.G., Kelsall, T., Leisawitz, D., & Weiland, J. 1998, COBE Diffuse Infrared Background Experiment Explanatory version 2.3, COBE Ref. Pub. No. 98-A (Greenbelt, MD: NASA GSFC), available in electronic form from the NSSDC at http://space.gsfc.nasa.gov/astro/cobe/dirbe_exsup.html

- Helou, G., Lu, N.Y., Werner, M.W., et al. 2000, *ApJ*, 532, L21
- Hong, S.S., & Greenberg, J.M. 1980, *A&A*, 88, 194
- Hony, S., van Kerckhoven, C., Peeters, E., et al. 2001, *A&A*, 370, 1030
- Hudgins, D.M., & Allamandola, L.J. 1995a, *J. Phys. Chem.*, 99, 3033
- Hudgins, D.M., & Allamandola, L.J. 1995b, *J. Phys. Chem.* 99, 8978
- Hudgins, D.M., & Allamandola, L.J. 1997, *J. Phys. Chem.* 101, 3472
- Hudgins, D.M., & Allamandola, L.J. 1999a, *ApJ*, 513, L69
- Hudgins, D.M., & Allamandola, L.J. 1999b, *ApJ*, 516, L41
- Hudgins, D.M., Bauschlicher, C.W., Allamandola, L.J., et al. 2000, *J. Phys. Chem.*, 104, 3655
- Hudgins, D.M., & Sandford, S.A. 1998a, *J. Phys. Chem.*, 102, 329
- Hudgins, D.M., & Sandford, S.A. 1998b, *J. Phys. Chem.*, 102, 344
- Hudgins, D.M., & Sandford, S.A. 1998c, *J. Phys. Chem.*, 102, 353
- Hudgins, D.M., Sandford, S.A., & Allamandola, L.J. 1994, *J. Phys. Chem.*, 98, 4243
- Hurwitz, M., Bowyer, S., & Martin, C. 1991, *ApJ*, 372, 167
- Joblin, C., Léger, A., & Martin, P. 1992, *ApJ*, 393, L79
- Joblin, C., Tielens, A.G.G.M., Allamandola, L.J., & Geballe, T.R. 1996a, *ApJ*, 458, 610
- Joblin, C., Tielens, A.G.G.M., Geballe, T.R., & Wooden, D.H. 1996b, *ApJ*, 460, L119
- Jochims, H.W., Rühl, E., Baumgärtel, H., Tobita, S., & Leach, S. 1994, *ApJ*, 420, 307
- Jones, A.P., Duley, W.W., & Williams, D.A. 1990, *QJRAS*, 31, 567
- Jones, A.P., & d'Hendecourt, L. 2000, *A&A*, 355, 1191
- Kim, S.H., Martin, P.G., & Hendry, P.D. 1994, *ApJ*, 422, 164
- Koch, E.E., Otto, A., & Radler, K. 1972, *Chem. Phys. Lett.*, 16, 131
- Kurtz, J. 1992, *A&A*, 255, L1
- Langhoff, S.R. 1996, *J. Phys. Chem.*, 100, 2819
- Lee, W., & Wdowiak, T.J. 1993, *ApJ*, 410, L127
- Léger, A., d'Hendecourt, L., & Défourneau, D. 1989a, *A&A*, 216, 148
- Léger, A., & Puget, J.L. 1984, *A&A*, 137, L5
- Léger, A., Verstraete, L., d'Hendecourt, L., et al. 1989b, in *Interstellar Dust (IAU Symposium 135)*, ed. L.J. Allamandola & A.G.G.M. Tielens (Dordrecht: Kluwer), 173

- Lepp, S., & Dalgarno, A. 1988, *ApJ*, 335, 769
- Li, A., & Draine, B.T. 2001, *ApJ*, 550, L213
- Li, A., & Greenberg, J.M. 1997, *A&A*, 323, 566
- Lillie, C.F., & Witt, A.N. 1976, *ApJ*, 208, 64
- Low, F.J., Young, E., Beintema, D., et al. 1984, *ApJ*, 278, L19
- Mathis, J.S. 1990, *ARA&A*, 28, 37
- Mathis, J.S. 1996, *ApJ*, 472, 643
- Mathis, J.S. 1998, *ApJ*, 497, 824
- Mathis, J.S., Mezger, P.G., Panagia, N. 1983, *A&A*, 128, 212
- Mathis, J.S., Ruml, W., & Nordsieck, K.H. 1977, *ApJ*, 217, 425
- Mathis, J.S., & Whiffen, G. 1989, *ApJ*, 341, 808
- Mattila, K., Lehtinen, K., & Lemke, D. 1999, *A&A*, 342, 643
- Mattila, K., Lemke, D., Haikala, L.K., et al. 1996, *A&A*, 315, L353
- Morgan, D.H., Nandy, K., & Thompson, G.I. 1976, *MNRAS*, 177, 531
- Moutou, C., Léger, A., & d'Hendecourt, L. 1996, *A&A*, 310, 297
- Moutou, C., Sellgren, K., Léger, A., Verstraete, L., & Le Coupanec, P. 1999, in *Solid Interstellar Matter: The ISO Revolution*, ed. L. d'Hendecourt, C. Joblin & A. Jones (New York: Springer), 90
- Moutou, C., Verstraete, L., Léger, A., Sellgren, K., & Schmidt, W. 2000, *A&A*, 354, L17
- Moutou, C., Verstraete, L., Sellgren, K., & Léger, A. 1999, in *The Universe as Seen by ISO*, ed. P. Cox & M. F. Kessler, ESA-SP427, 727
- Omont, A. 1986, *A&A*, 164, 159
- Onaka, T., Yamamura, I., Tanabe, T., et al. 1996, *PASJ*, 48, L59
- Papoular, R., Ellis, K., Guillois, O., Reynaud, C., & Nenner, I. 1993, *J. Chem. Soc. Farady Trans.*, 89, 2289
- Pauzat, F., Talbi, D., & Ellinger, Y. 1997, *A&A*, 319, 318
- Platt, J.R. 1956, *ApJ*, 123, 486
- Reach, W.T., Boulanger, F., Contursi, A., & Lequeux, J. 2000, *A&A*, 361, 895
- Reach, W.T., Dwek, E., Fixsen, D.J., et al. 1995, *ApJ*, 451, 188
- Robin, M.B. 1975, *Higher Excited States of Polyatomic Molecules*, Vol. II (London: Academic Press)
- Roche, P.F., Aitken, D.K., & Smith, C.H. 1989, *MNRAS*, 236, 485
- Roche, P.F., Lucas, P.W., Hoare, M.G., Aitken, D.K., & Smith, C.H. 1996, *MNRAS*, 280, 924

- Roelfsema, P.R., Cox, P., Tielens, A.G.G.M., et al. 1996, *A&A*, 315, L289
- Sakata, A., Wada, S., Onaka, T., & Tokunaga, A.T. 1990, *ApJ*, 353, 543
- Salama, F., Bakes, E.L.O., Allamandola, L.J., et al. 1996, *ApJ*, 458, 621
- Schutte, W.A., Tielens, A.G.G.M., & Allamandola, L.J. 1993, *ApJ* 415, 397
- Schutte, W.A., van der Hucht, K.A., Whittet, D.C.B., et al. 1998, *A&A*, 337, 261
- Scott, A., Duley, W.W., & Pinho, G.P. 1997, *ApJ*, 489, L193
- Sellgren, K., Brooke, T.Y., Smith, R.G., & Geballe, T.R. 1995, *ApJ*, 449, L69
- Sellgren, K., Werner, M.W., & Allamandola, L.J. 1996, *ApJS*, 102, 369
- Sellgren, K., Werner, M.W., & Dinerstein, H.L. 1983, *ApJ*, 271, L13
- Siebenmorgen, R., & Krügel, E. 1992, *A&A*, 259, 614
- Snow, T.P., & Witt, A.N. 1995, *Science*, 270, 1455
- Stecher, T.P. 1965, *ApJ*, 142, 1683
- Stein, S.E., & Brown, R.L. 1991, *J. Am. Chem. Soc.*, 113, 787
- Sturm, E., Lutz, D., Tran, D., et al. 2000, *A&A*, 358, 481
- Szczepanski, J., & Vala, M. 1993, *ApJ*, 414, 646
- Szczepanski, J., Wehlburg, C., & Vala, M. 1995, *Chem. Phys. Lett.*, 232, 221
- Tanaka, M., Matsumoto, T., Murakami, H., et al. 1996, *PASJ*, 48, L53
- Tielens, A.G.G.M., Allamandola, L.J., Barker, J.R., & Cohen, M. 1987, in *Polycyclic Aromatic Hydrocarbons and Astrophysics*, ed. A. Léger, L. d'Hendecourt, & N. Boccara (Dordrecht: Reidel), 273
- Tielens, A.G.G.M., Hony, S., van Kerckhoven, C., & Peeters, E. 1999, in *The Universe as Seen by ISO*, ed. P. Cox & M. F. Kessler, ESA-SP427, 579
- Tokunaga, A.T., Sellgren, K., Smith, R.G., et al. 1991, *ApJ*, 380, 452
- Trumpler, R.J. 1930, *PASP*, 42, 214
- Uchida, K.I., Sellgren, K., & Werner, M.W. 1998, *ApJ*, 493, L109
- Uchida, K.I., Sellgren, K., Werner, M.W., & Houdashelt, M.L. 2000, *ApJ*, 530, 817
- UV Atlas 1966, *UV Atlas of Organic Compounds* (New York: Plenum Press)
- van der Zwet, G.P., & Allamandola, L.J. 1985, *A&A*, 146, 76
- Verstraete, L., Pech, C., Moutou, C., et al. 2001, *A&A*, in press
- Verter, F., Magnani, L., Dwek, E., & Rickard, L.J. 2000, *ApJ*, 536, 831
- Webster, A. 1993, *MNRAS*, 264, 121

- Weiland, J.L., Blitz, L., Dwek, E., et al. 1986, *ApJ*, 306, L101
- Weingartner, J.C., & Draine, B.T. 2001a, *ApJ*, 548, 296 (WD01a)
- Weingartner, J.C., & Draine, B.T. 2001b, *ApJS*, 134, 263
- Weingartner, J.C., & Draine, B.T. 2001c, *ApJ*, 553, 581
- Witt, A.N. 2000, in *Astrochemistry: From Molecular Clouds to Planetary Systems* (IAU Symposium 197), ed. E.F. van Dishoeck, (Dordrecht: Kluwer), in press
- Witt, A.N., Friedmann, B.C., & Sasseen, T.P. 1997, *ApJ*, 481, 809
- Witteborn, F.C., Sandford, S.A., Bregman, J.D., et al. 1989, *ApJ*, 341, 270
- Wright, E.L., Mather, J.C., Bennett, C.L., et al. 1991, *ApJ*, 381, 200
- Zubko, V.G. 1999, in *Formation and Evolution of Solids in Space*, ed. J.M. Greenberg & A. Li (Dordrecht: Kluwer), 85